CALPHAD: Computer Coupling of Phase Diagrams and Thermochemistry 90 (2025) 102848

Contents lists available at ScienceDirect

Calphad

journal homepage: www.elsevier.com/locate/calphad

Modified polyhedron model for predicting standard enthalpy of formation and entropy of mixed oxides

Jesus A. Arias Hernandez, Elmira Moosavi-Khoonsari *

Department of Mechanical Engineering, École de Technologie Supérieure (ÉTS), 1100 Notre-Dame St W, Montreal, Quebec, H3C 1K3, Canada

ARTICLE INFO

Handling Editor: Prof. Z.K. Liu

Keywords:
Thermodynamic property estimation
Standard entropy and enthalpy of formation
Mixed oxides
Polyhedron model
Machine learning
Neural network

ABSTRACT

Thermodynamic modeling of oxidic systems is crucial in advancing various fields of science and technology. Polyhedron Model (PM) estimates the standard enthalpy of formation and entropy of mixed oxides via the linear summation of the thermodynamic properties of constituent polyhedra. Each polyhedron consists of a centered cation with neighboring oxygen anions; hence, the model accounts for the interaction between anions and cations. While second-order transitions have been considered in previous iterations of the model, the PM has certain shortcomings, including neglect of variations in polyhedron volume, polyhedron distortion, inter-polyhedron linkage, and second nearest-neighbor or higher-order interactions, which are not negligible. The present work introduces the Modified Polyhedron Model (MPM), which aims to incorporate these contributions through a neural network (NN) model to improve the accuracy of predictions for standard enthalpy of formation ($\Delta H^{o}_{298\ K}$) and standard entropy ($S^{o}_{298\ K}$). This is possible by using the residuals from the PM as inputs to the NN model, whose outputs are the calculated thermodynamic properties of compounds. The dataset consists of 155 compounds in the Li-Na-K-Ca-Mg-Mn-Fe-Al-Ti-Si-O system, classified by 20 polyhedra. The MPM considerably reduces the error in predicting enthalpy of formation and entropy, improving the alignment with experimental values across most analyzed compounds in comparison with the PM. These results suggest that the MPM can significantly improve the predictability of thermodynamic properties for mixed oxides.

1. Introduction

Knowledge of the thermodynamic properties of oxides, including enthalpy of formation ($\Delta H^{o}_{298\ K}$) and standard entropy ($S^{o}_{298\ K}$) is crucial for analyzing multicomponent chemical reactions and phase equilibria in various fields such as ceramics [1,2], glassmaking [3,4], pyrometallurgy [5,6], and geology. For example, the Mineralogical Society of America's handbook of mineralogy lists 5663 species, many of which are oxides [7]. However, thermodynamic data are available for only about 1100 and a full thermodynamic description for only a few hundred. Many of these properties remain unknown due to experimental challenges, such as volatility, hygroscopic behavior, and lengthy equilibration times required for their synthesis [8].

Theoretical models based on ab initio calculations, such as Density Functional Theory (DFT) [9,10] and Molecular Dynamics (MD) [11–13], are an active area of research. Besides both being computationally demanding [14], DFT struggles to predict thermodynamic properties at temperatures different from 0 K. In the Born-Oppenheimer DFT approach, nuclei are assumed to be fixed, which impacts the calculation of temperature-dependent properties. On the other hand, Kohn-Sham DFT requires tracking many high-energy electronic states to account for thermal effects, which makes calculations extremely impractical [15]. Empirical models have also been proposed to predict thermodynamic properties. These models use group contribution-based methods such as a summation of constituent elements [16], oxides [16–18], iso-structural minerals [19], or components defined by their coordination numbers [20–25]. Most of the proposed empirical models are based on additivity rules, modifications of structural analogs, or linear regression-based correlations between thermodynamic properties and structural data. The empirical approach makes them less computationally expensive and, therefore, more easily applied to the prediction of unknown enthalpy [26–29] and entropy [16,30,31]. Among them, the Neumann-Kopp Rule (NKR) is widely used to calculate $S^{o}_{298\ K}$. This model is based on the simple addition of the thermodynamic properties of constituent oxides, and is used as a first approximation [17].

The Polyhedron Model (PM) was first used by Robinson and Hass [32] to estimate the thermodynamic properties of constituent polyhedra of silicate minerals and subsequently calculate their thermodynamic

* Corresponding author.
E-mail address: Elmira.moosavi@etsmtl.ca (E. Moosavi-Khoonsari).

https://doi.org/10.1016/j.calphad.2025.102848
Received 7 March 2025; Received in revised form 7 May 2025; Accepted 14 June 2025
Available online 26 June 2025

properties. PM extends Pauling's rules for atomic arrangement in crystals with ionic bonding and builds on the idea that First Nearest Neighbor (FNN) bonding plays a crucial role in determining the structure and properties of ionic crystals [33]. PM is based on two key assumptions [1]: ionic compounds can be divided into constituent polyhedra, i.e., coordination sites where cations are bonded to surrounding anions, which retain consistent properties across different compounds, and [2] the thermodynamic properties of an ionic compound can be estimated by the linear summation of the thermodynamic properties of its constituent polyhedra.

There are important features underestimated by the PM such as [1]: the polyhedron volume (i.e., the volume of a specific polyhedron may vary across different compounds) [2], the polyhedron distortion (i.e., a regular polyhedron is defined as a cluster with all anion-anion edges of the same length and all anion-cation angles equal, which is not necessarily present in every compound) [3], the inter-polyhedron linkage (i.e., "linkage rigidity" depends on the shared anions among polyhedra) [4], the excess mixing properties (i.e., the PM is simply based on mechanical mixing of polyhedra and Second Nearest Neighbors (SNN) or longer-range interactions are not considered), and [5] the second-order transitions (i.e., the magnetic and cation site order-disorder transitions are important contributions in some compounds) [33]. Additionally, the PM is only applicable in ionic compounds that can be divided into distinct polyhedra (e.g., it cannot be applied to covalent sulfides and sulfosalts) [33–35].

Holland et al. [21] improved the PM by incorporating volume-corrected entropy and second-order transition contributions, such as cation site and magnetic order-disorder transitions [36]. The model was further expanded by Iglesia et al. [37] to predict the entropy of carbonate minerals. Hinsberg et al. [22,23] also determined the thermodynamic properties for 35 polyhedra, considering second-order transition contributions, and concluded that the molar volume corrections had no impact on the entropy results. Wu et al. [24] expanded the model by including 48 silicates and 19 titanates and considering second-order transition contributions, found that including molar volume into the entropy slightly improved the prediction by 0.10 %. The PM demonstrated promise in estimating the standard enthalpy of formation and entropy of mixed oxides within ±0.56 % and 3.50 % error ranges, respectively.

Since the time of Holland [21] and the incorporation of volume-corrected entropy and the second-order transition contributions into the PM, there have been no improvements to the model structure to address its limitations. The linearly regressed residuals from the PM may provide insights into the overlooked features [23,33,35]. Machine learning (ML) models have enhanced predictions of physical properties, such as transition and decomposition temperatures of inorganic compounds [38,39]. The present work focuses on developing the next generation of PM, i.e., the Modified Polyhedron Model (MPM), for enhancing the prediction of standard enthalpy of formation and entropy of mixed oxides by incorporating a non-linear model into the PM. A neural network (NN) model is used to increase the PM predictability by taking the residuals of the PM as inputs.

2. Methodology

2.1. Polyhedron model

The PM assumes that thermodynamic properties can be calculated from the linear summation of the thermodynamic properties of their constituent polyhedra [32]. Therefore, the thermodynamic properties of mixed oxides can be calculated using Equations [1,2]:

$$\Delta H^{o}_{298\ K,i} = \sum n_{\{i,j\}} \Delta H_{298\ K,j} \tag{1}$$

$$S^{o}_{298\ K,i} = \sum n_{\{i,j\}} S_{298\ K,j} \tag{2}$$

where $\Delta H^{o}_{298\ K}$ and $S^{o}_{298\ K}$ are the standard enthalpy of formation and entropy, i is the ionic compound, j is the constituent polyhedra and $n_{\{i,j\}}$ is the stoichiometry of the constituent polyhedra. The thermodynamic properties of polyhedra can then be estimated by linear regression based on the properties of compounds that contain these polyhedra.

2.2. Second-order transition contributions

Oxides may contain second-order transition contributions such as those caused by magnetic and cation site order-disorder, which affect their thermodynamic properties. Second-order transitions are often characterized by a sharp peak in heat capacity (C_P) curves at a specific critical temperature (T_c), indicating a significant increase in the energy required to raise the temperature. These contributions cannot be considered by PM, and if not extracted, they may lead to a decrease in its predictability. Magnetic order-disorder transitions are commonly observed in oxides containing transition metals, such as Fe^{2+}, Fe^{3+}, and Mn^{2+} [23,24,40]. This type of transition can occur at temperatures below room temperature, as seen in $Ca_3Fe_2Si_3O_{12}$ [41], $CaFeSi_2O_6$ [42], and $Fe_2Si_2O_6$ [43], or above room temperature, as in the cases of magnetite (Fe_3O_4) [44], and hematite (Fe_2O_3) [45]. The cation site order-disorder is related to changes in the distribution of cations within the same crystal sublattice structure [36] and often occurs at high temperatures [46].

The ideal excess contributions to entropy arising from phenomena other than vibrational effects, such as magnetic ($S^{magnetic}_{max}$) and site order-disorder (S^{site}_{max}) [47], can be calculated using Equations [3,4], respectively [28]:

$$S^{magnetic}_{max} = R \sum n\ In\ (2s+1) \tag{3}$$

$$S^{site}_{max} = -mR \sum X_i \ln X_i \tag{4}$$

where s is the spin quantum number: 2, 5/2 and 5/2 for Fe^{2+}, Fe^{3+} and Mn^{2+}, respectively, R is the gas constant, and n is the number of moles of Fe^{2+}, Fe^{3+}, and Mn^{2+} in the compound. Also, m is the multiplicity of the sublattice site where the cation mixing can occur, and X_i is the mole fraction of species i in a specific sublattice.

For oxides with critical temperatures below 298 K, the maximum (ideal) contributions to enthalpy of formation and entropy resulting from second-order transitions must be considered for the calculation of thermodynamic properties of polyhedra. These contributions can be calculated using Equations [5,6,21,48]:

$$\Delta H_{max} = \frac{2}{3}\left(S^{magnetic}_{max} T_{c,mag} + S^{site}_{max} T_{c,sit}\right) \quad T \le 298\ K \tag{5}$$

$$S_{max} = S^{magnetic}_{max} + S^{site}_{max} \quad T \le 298\ K \tag{6}$$

where $T_{c,mag}$ and $T_{c,sit}$ are the critical temperatures such as Curie, Néel, and site disorder temperatures, respectively, in Kelvin.

For oxides with critical temperatures above 298 K, contributions related to second-order transitions are calculated using Landau Theory, as proposed by Holland [21], and can be expressed using Equations [7,8]:

$$\begin{aligned}\Delta H^{ex}_{-298K} = &\left(2S^{magnetic}_{max} T_{c,mag}\right)\left(\frac{(Q_{mag})^6}{6} - \frac{(Q_{mag})^2}{2} - \frac{1}{3}\right) \\ &+ \left(2S^{site}_{max} T_{c,sit}\right)\left(\frac{(Q_{sit})^6}{6} - \frac{(Q_{sit})^2}{2} - \frac{1}{3}\right) \quad T \ge 298\ K\end{aligned} \tag{7}$$

$$S^{ex}_{-298K} = S^{magnetic}_{max}\left(1 - (Q_{mag})^2\right) + S^{site}_{max}\left(1 - (Q_{sit})^2\right) \quad T \ge 298\ K \tag{8}$$

where:

$$Q_{mag} = \left(1 - \frac{298.15}{T_{c,mag}}\right)^{\frac{1}{4}} \quad (9)$$

$$Q_{dis} = \left(1 - \frac{298.15}{T_{c,sit}}\right)^{\frac{1}{4}} \quad (10)$$

2.3. Data pre-processing

Data preprocessing was performed in three main steps [1]: data splitting for training, cross-validation, and testing of the PM and MPM [2]; calculation of the residuals from the PM; and [3] data scaling for the NN models.

2.3.1. Data splitting

The data were split after subtracting the excess properties. It was randomly divided into 90 % for training and cross-validation (i.e., the train set), and 10 % for testing. This approach ensures that as much data as possible is retained for the training set, while also providing a representative sample for model evaluation on the test set. The 90 % training data were further divided into 10 random folds to facilitate cross-validation during the hyperparameter optimization process.

2.3.2. Residuals from PM

The residuals from the PM, $\Delta H^0_{298\ K,res}$ and $S^0_{298\ K,res}$ (where '*res*' denotes residuals) serve as input data for the NN model. They were calculated by subtracting the back-calculated values from the PM (here, $\Delta H^0_{298\ K,PM}$ and $S^0_{298\ K,PM}$) from the corresponding dataset values ($\Delta H^0_{298\ K,dataset}$ and $S^0_{298\ K,dataset}$), as given in Table A in the appendix, using Equations [11,12]:

$$\Delta H^0_{298\ K,res} = \Delta H^0_{298\ K,dataset} - \Delta H^0_{298\ K,PM} \quad (11)$$

$$S^0_{298\ K,res} = S^0_{298\ K,dataset} - S^0_{298\ K,PM} \quad (12)$$

2.3.3. Data scaling

Scaling in NN models is often used to improve the training process and overall performance. Faster convergence is achieved by scaling the inputs into a consistent range, which also prevents the dominance of larger values in the dataset, which could lead to poor learning [49]. In the present work, a standard scaler was used in the feature matrix (i.e., polyhedra) for the training and cross-validation processes, as explained by Equation [13]:

$$z = \frac{x - u}{s} \quad (13)$$

where z is the standard score, x is the sample value, u is the mean of the training samples and s is the standard deviation of the training samples. This was repeated for the 18 features, each corresponding to a different polyhedron. The use of a standard scaler in the feature matrix ensures that each feature contributes equally to the training of the model.

For the output features (i.e., thermodynamic properties) in the training and cross-validation steps, a Min-Max type scaler was used, described by Equation [14]:

$$z = \frac{10\,x}{x_{max} - x_{min}} \quad (14)$$

where x_{min} and x_{max} are the minimum and maximum values of the output values, and x is the currently scaled sample. The min-max type scaler used for the output features helps keep the output values within a fixed range and avoids a larger distribution range.

2.4. Neural network model

Neural networks are a class of ML models that consist of layers of interconnected nodes (neurons) that process the input weights, a bias, and transform them to produce an output. Each node receives as inputs either the input data for the first layer or the data processed as a weighted sum from the previous layer outputs. Each input is associated with a weight that indicates how much influence a particular input has on the node's output. The weighted sum is transformed by an activation function, which introduces non-linearity into the model, and the result of the activation function determines the node's output [50]. In the present work, the selected activation function for the input and hidden layers is the hyperbolic tangential function (Tanh), where $y = \tanh(x)$, as it is capable of considering both positive and negative values from the features. For the output layer, a linear activation function ($y = x$) was selected. During training, the model produces an output, and a loss function calculates the error between the predicted output and the dataset value. The network then adjusts the weights associated with each node through backpropagation, which involves computing the gradient of the loss function with respect to each weight and using optimization techniques to update the weight in a direction that minimizes the error. The selected optimizer in this work is Adam (Adaptive Momentum), which has been shown to be robust in many works for different areas of science and engineering [51].

2.4.1. Hyperparameter optimization and cross validation

Hyperparameter optimization involves selecting the best combination of hyperparameters, such as the learning rate, number of hidden layers, and number of neurons, that yields the best performance. In the present work, a grid search method was used to optimize the NN architecture and learning rate. The learning rate was varied between 1×10^{-3} and 1×10^{-4}, while the number of hidden layers was set to 2, 3, and 4. Additionally, each hidden layer consisted of 8, 16, 32, 64, and 128 neurons. Combining these parameters, a total of 30 NN models were tested for each thermodynamic property, as shown in Fig. 1.

To obtain improved hyperparameters through iteration, a cross-validation step was conducted for each architecture. This approach consists of randomly splitting the train set into multiple folds, and the model is then trained by excluding different folds each time [49,52]. For example, in a 10-fold cross-validation approach, the model will be trained with 9 of the 10 folds, and the remaining fold will be used for validation. This method is often used to prevent overfitting by evaluating how well the model generalizes to unseen data. A model that performs well on the training data but poorly on the validation set is likely overfitting [52,53].

2.5. Evaluation metrics

To evaluate the results produced at each step of the MPM, different metrics need to be used. The coefficient of determination, denoted as R^2, measures how well the observed outcomes are replicated by the model. It is calculated as shown in Equation [15]:

$$R^2 = 1 - \frac{\sum_i (y_i - \hat{y}_i)^2}{\sum_i (y_i - \bar{y}_i)^2} \quad (15)$$

where y_i are the real values, $\hat{y}_i$ are the values calculated by the model, and $\bar{y}_i$ is the calculated mean of the real values.

The Mean Absolute Error (MAE) is the arithmetic average of the absolute errors. The calculated MAE uses the same scale as the data being analyzed. It is represented by Equation [16]:

$$MAE = \frac{\sum_i |y_i - \hat{y}_i|}{n} \quad (16)$$

Mean Square Error (MSE) measures the average of the squares of the errors, while RMSE is the square root of MSE, providing an error metric with the same units as the analyzed data. These metrics are more

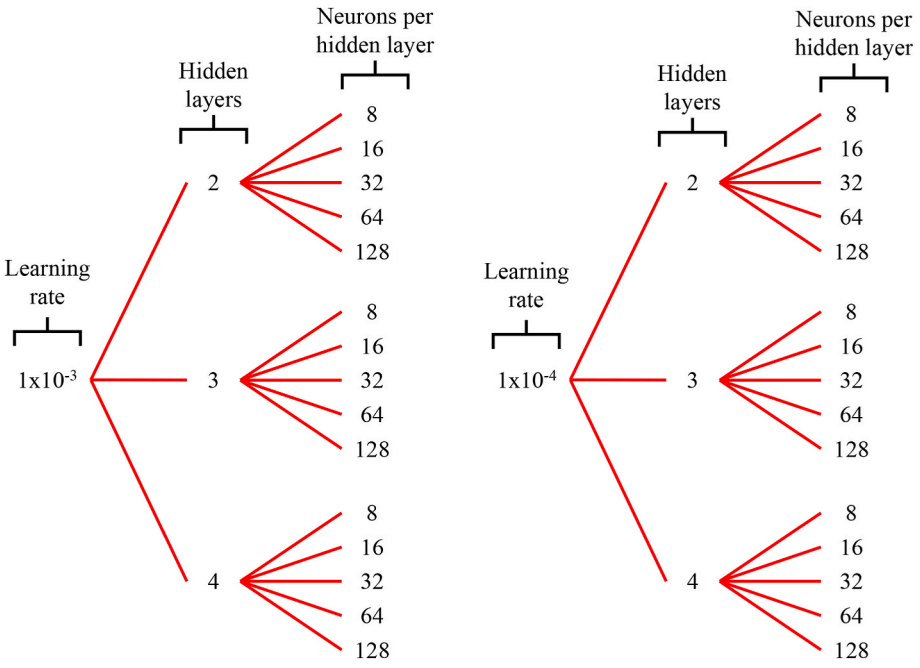

Fig. 1. Grid search representation of the neural network models used for each thermodynamic property.

sensitive to outlier values. They are calculated using Equations [17,18]:

$$MSE = \frac{\sum_i (y_i - \hat{y}_i)^2}{n} \tag{17}$$

$$RMSE = \sqrt{MSE} \tag{18}$$

2.6. Prediction of output enthalpy of formation and entropy

For the prediction of thermodynamic properties of a new compound, three main contributions are required [1]: linear contributions, arising from lattice vibrations and can be calculated using PM, denoted as $\Delta H^0_{298\ K,PM}$ and $S^0_{298\ K,PM}$ [2]; non-linear contributions, corresponding to polyhedron volume, distortion, linkage, and mixing properties, calculated by the NN, denoted as $\Delta H^0_{298\ K,res}$ and $S^0_{298\ K,res}$; and [3] second-order transitions, which account for magnetic and cation site order-disorder effects (i.e., ΔH_{max}, S_{max}, ΔH^{ex}_{-298K}, S^{ex}_{-298K}). Therefore, enthalpy of formation and entropy can be expressed as follows:

$$\Delta H^0_{298\ K} = \Delta H^0_{298\ K,PM} + \Delta H^0_{298\ K,res} + \Delta H_{max} + \Delta H^{ex}_{-298K} \tag{19}$$

$$S^0_{298\ K} = S^0_{298\ K,PM} + S^0_{298\ K,res} + S_{max} + S^{ex}_{-298K} \tag{20}$$

3. Results

3.1. Modified polyhedron model

Fig. 2 displays the sequential steps for developing the MPM, which consists of two main parts: the traditional PM and the newly developed NN model. The PM involves calculating the intrinsic thermodynamic properties of polyhedra via multiple linear regression using the corresponding thermodynamic properties of compounds included in the train set. The NN model includes data splitting and scaling, cross-validation for hyperparameter optimization, and training of the NN using the full train set.

3.2. Data collection

One hundred fifty-five mixed oxides (binary and ternary) were selected from the Li-Na-K-Ca-Mg-Mn-Fe-Al-Ti-Si-O system for the present work. The thermodynamic properties were collected from FactSage 8.2 databases (i.e., FToxid, FactPS) and Hinsberg et al. [23] The $\Delta H^0_{298\ K}$ and $S^0_{298\ K}$ values are listed in Table An under the columns labeled "Database". Additionally, the number of atoms per formula unit for each compound is included in Table A. The excess values of enthalpy and entropy were calculated using equations [5–10] based on the T_c found in literature (See Table A in the appendix). Therefore, the values of enthalpy of formation and entropy calculated after extracting the excess properties using equations [21,22], respectively, are included in Table An under the label "Dataset".

$$\Delta H^0_{298\ K,dataset} = \Delta H^0_{298\ K} - \Delta H_{max} - \Delta H^{ex}_{-298K} \tag{21}$$

$$S^0_{298\ K,dataset} = S^0_{298\ K} - S_{max} - S^{ex}_{-298K} \tag{22}$$

The compounds were classified into 18 polyhedra based on their crystal sub-lattice structures (see Table B in the appendix). The polyhedra were used as the feature matrix for the NN model, resulting in 18 features.

3.3. Polyhedron model results

As explained in Section 2, this work uses the PM to first approximate the thermodynamic properties of polyhedra and calculate the residuals that serve as inputs for the NN models. Since the PM is based on the linear summation of constituent polyhedra, it is possible to calculate the properties of each polyhedron using linear regression. The derived polyhedron thermodynamic properties are provided in Table 1, along with the Standard Error (SE) of the coefficients, which serves as an indicator of the uncertainty associated with estimating the values of each coefficient [23,54].

3.4. Hyperparameter optimization

A grid search methodology was used to identify our best hyperparameters (e.g., hidden layers, number of neurons, learning rate), and the results were evaluated using the MSE metric [49]. Fig. 3 shows the hyperparameter optimization results for $\Delta H^0_{298\ K,res}$ and $S^0_{298\ K,res}$. By

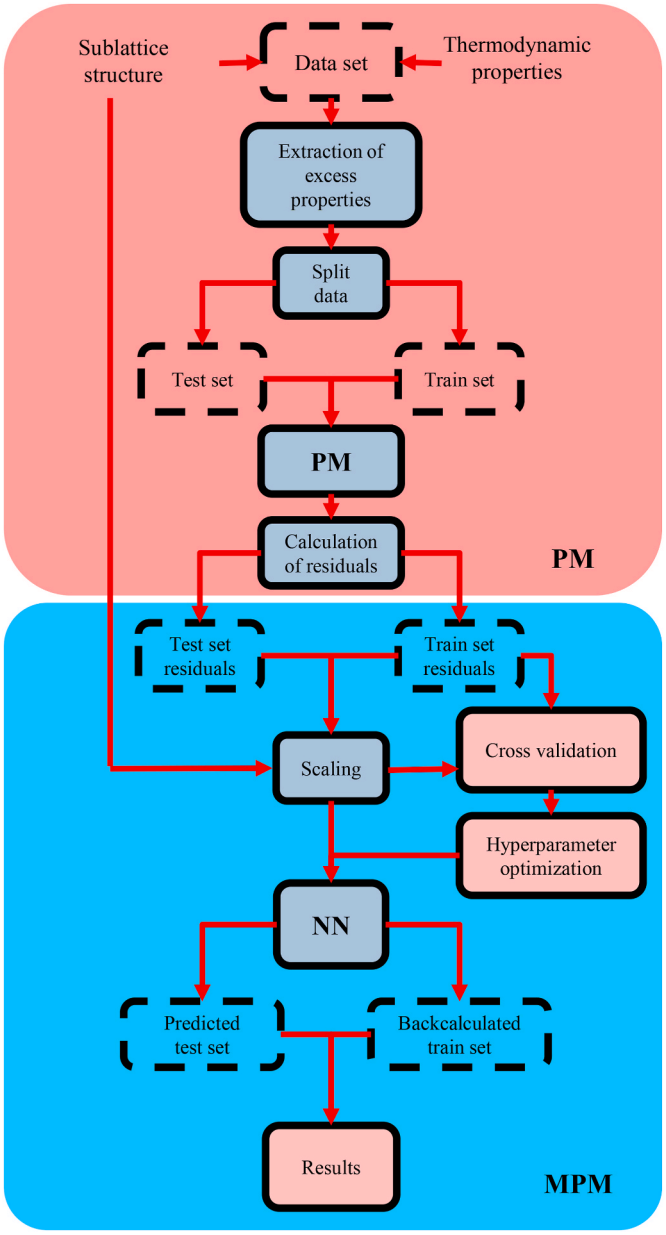

Fig. 2. Flowsheet for the Polyhedron Model (PM) and the modifications performed in the present work, i.e., the Modified Polyhedron Model (MPM).

comparing Fig. 3(a) and (b), it is observed that the lowest MSE for $\Delta H^0_{298\ K,res}$ cross-validation is achieved with 3 hidden layers, 32 neurons per hidden layer, and a learning rate of 1×10^{-4}. For $S^0_{298\ K,res}$ cross-validation, the best conditions are found using 2 hidden layers, each with 128 neurons, and a learning rate of 1×10^{-4} (see Fig. 3(c) and (d)). It is also worth noting that for both $\Delta H^0_{298\ K,res}$ and $S^0_{298\ K,res}$, a lower learning rate resulted in better performance, regardless of the NN architecture.

3.5. Modified polyhedron model

Fig. 4 compares the PM and MPM for back-calculation of the train set and prediction of the test set for $\Delta H^0_{298\ K}$ and $S^0_{298\ K}$ using our optimal architectures identified during hyperparameter optimization. For enthalpy of formation prediction, the PM shows the following metrics: $R^2 = 99.83$ %, MAE: 85.57 kJ mol^{-1}, MSE: 11.13×10^6 $\left(\text{kJ mol}^{-1}\right)^2$, and RMSE: 106.64 kJ mol^{-1}, while the MPM shows the following metrics: $R^2 = 99.94$ %, MAE = 51.67 kJ mol^{-1}, MSE = 4.11×10^6 $\left(\text{kJ mol}^{-1}\right)^2$, and RMSE = 64.18 kJ mol^{-1} (see Fig. 4(a)). This indicates that the MPM reduced the MAE by 40 %, the MSE by 64 % and the RMSE by 40 %. For the entropy prediction, the metrics for the PM are: R^2 = 94.14 %, MAE = 17.07 J mol^{-1} K^{-1}, MSE = 462.54 (J mol^{-1} K^{-1})^2, and RMSE = 21.51 J mol^{-1} K^{-1}, while for the MPM, the metrics are: $R^2 = 97.48$ %, MAE = 9.83 J mol^{-1} K^{-1}, MSE = 199.13 $\left(\text{J mol}^{-1}\text{ K}^{-1}\right)^2$, and RMSE = 14.11 J mol^{-1} K^{-1}. In the case of the entropy, the errors for the MPM were lower, with MAE reduced by 42 %, MSE by 57 %, and RMSE by 34 %. The improvement in the metrics for both entropy and enthalpy of formation predictions suggests that the MPM provides more accurate results compared to the PM.

Table 1
Calculated enthalpy and entropy values for polyhedra and their standard error coefficient, obtained from the PM.

Polyhedra	$\Delta H_{298\ K}$ $\left(J\ mol^{-1}\right)$	$\Delta H_{298\ K}$ SE	$S_{298\ K}$ $\left(J\ mol^{-1}\ K^{-1}\right)$	$S_{298\ K}$ SE
Ti-oct	−971,734	8424	49.98	1.55
Si-tet	−943,546	6008	42.12	1.10
Al-tet	−820,990	10,590	29.32	1.94
Al-oct	−832,110	10,976	28.16	2.01
Fe3+-oct	−391,021	12,863	50.45	2.36
Fe-tet	−318,517	58,181	41.70	10.70
Fe-oct	−269,696	24,458	43.38	4.49
Mn-tet	−369,908	91,465	45.40	16.80
Mn-oct	−455,059	13,496	56.02	2.48
Mg-tet	−604,846	24,784	28.14	4.55
Mg-oct	−613,754	14,829	25.61	2.72
Ca-oct	−686,195	20,171	44.91	3.70
Ca-multi	−692,760	8372	38.38	1.54
Li-tet	−329,563	17,133	20.95	3.14
Li-oct	−402,856	64,844	19.30	11.90
Li-multi	−330,589	11,107	19.49	2.04
Na-multi	−263,768	6643	43.91	1.22
K-multi	−282,861	8996	53.54	1.65

Furthermore, larger errors observed in the PM train set compared to the PM test set, as seen in Fig. 4(b), can be attributed to the specific characteristics of the compounds randomly assigned to each set to avoid selection bias. As such, the train set may include compounds with more complex structural features, such as highly distorted polyhedra or unusually weak or strong linkages between polyhedra, while the test set may contain compounds with more regular, average behavior. Since the PM model does not explicitly account for such deviations from average structural characteristics, higher residuals in the train set are to be expected in such cases.

4. Discussion

4.1. Residual analysis

Fig. 5 compares the residuals of both the PM and MPM, normalized by the number of atoms in each compound (where the total number of atoms, N_{Atoms}, is the sum of cations and anions: $\left(N_{Atoms} = \sum_{i>1} N_{C_i} + N_{O^{2-}}\right)$. This normalization ensures that the data is not skewed by larger molecules and highlights clear patterns. In the present work, the MPM and PM have been applied only to mixed oxides (i.e., oxides containing

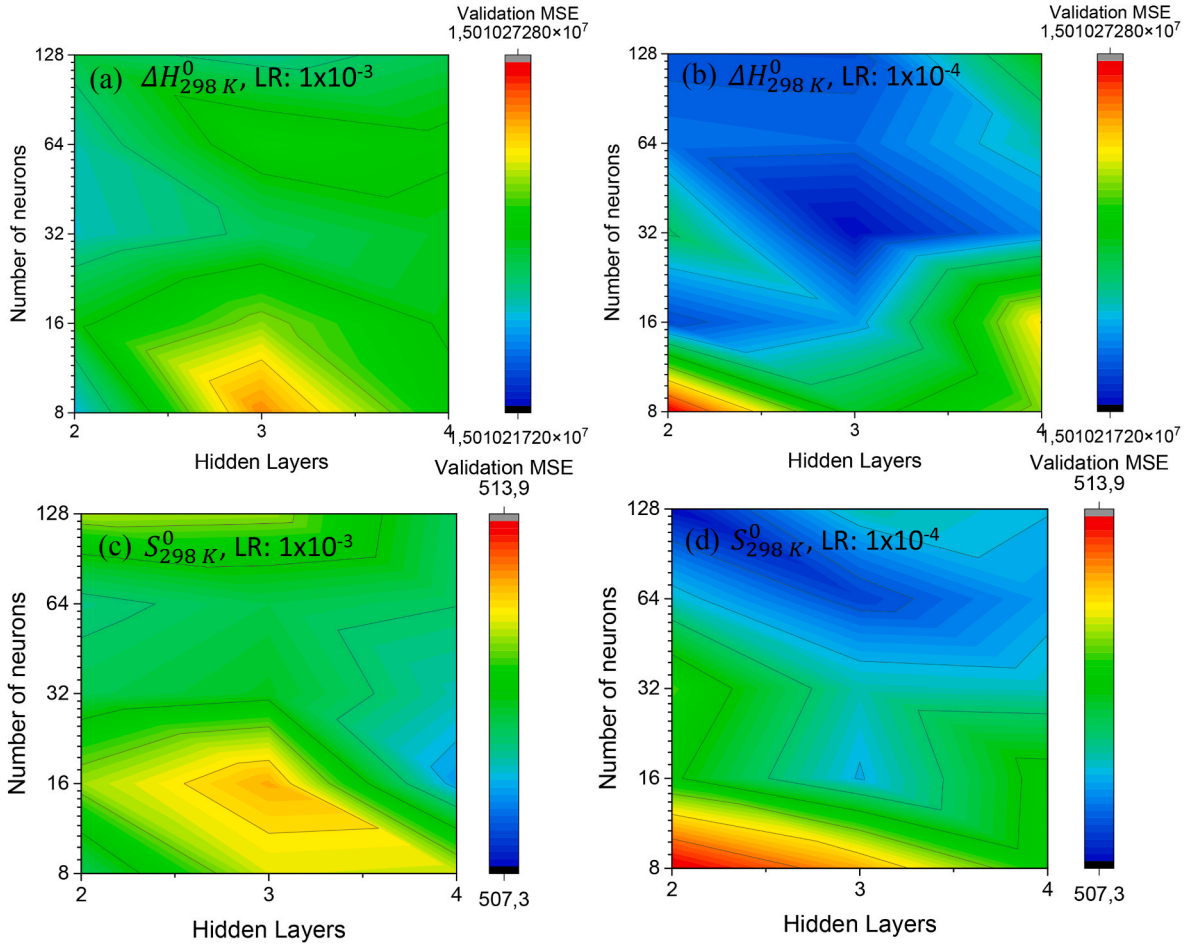

Fig. 3. Grid search for hyperparameter optimization of NN models: average MSE for (a) $\Delta H^0_{298\,K,res}$ cross-validation with learning rate of 1×10^{-3}, (b) $\Delta H^0_{298\,K,res}$ cross-validation with learning rate of 1×10^{-4}, (c) $S^0_{298\,K,res}$ cross-validation with learning rate of 1×10^{-3}, and (d) $S^0_{298\,K,res}$ cross-validation with learning rate of 1×10^{-4}.

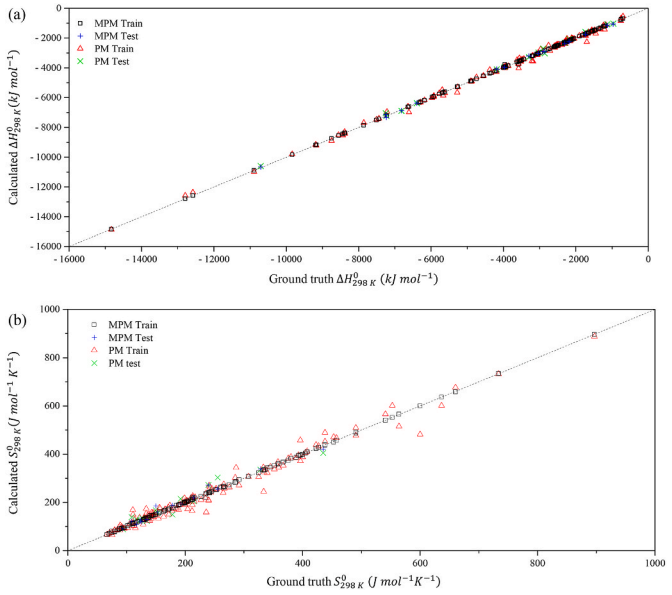

Fig. 4. Scatter plots comparing back-calculations from the train set and predictions from the test set with ground truth values: (a) enthalpy of formation, (b) entropy, for both PM and MPM (Ground truth represents all data used for training and testing).

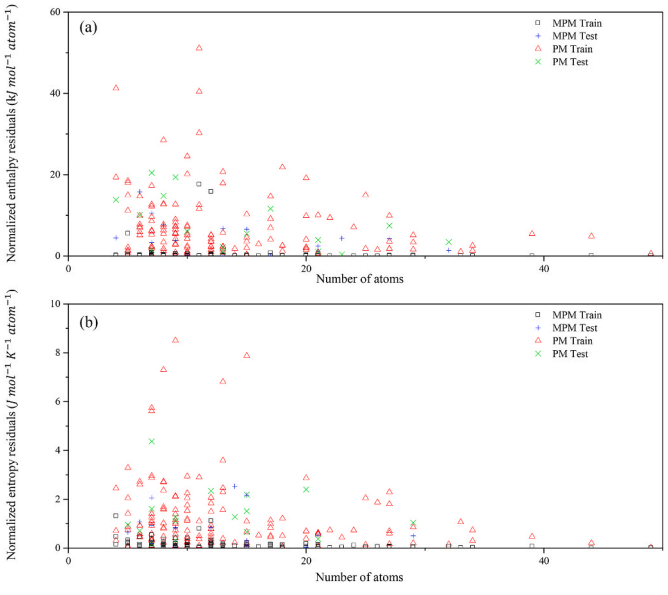

Fig. 5. Comparison of normalized residuals between PM and MPM: (a) enthalpy of formation and (b) entropy, calculated using the models developed in this work.

at least two different types of polyhedra. There is no limitation regarding the minimum or maximum number of atoms. However, the minimum number of atoms in the dataset for the present work happened to be five. As seen in Fig. 5, the residuals tend to increase with fewer atoms. As explained by Arias et al. [25] for PM, this behavior could be attributed to the increased significance of second and higher-order cation-cation interactions in smaller compounds. Such effects were considered by implementing an NN in MPM, reducing the residuals. It should also be noted that for a higher number of atoms, even though the error decreases, the availability of the data is very limited.

In Fig. 5(a), the highest residuals for the train set in terms of enthalpy of formation decreased significantly from 51 kJ mol $^{-1}$ atom^{-1} in the PM to less than 18 kJ mol $^{-1}$ atom^{-1} in the MPM. With the exception of $Ca_3Ti_2O_6$ ($3CaO{\cdot}Ti_2O_3$) and $Ca_3Ti_2O_7$ ($3CaO{\cdot}2TiO_2$), the residuals back-calculated from the MPM were less than 15.83 kJ mol $^{-1}$ atom^{-1}. $Ca_3Ti_2O_6$ and $Ca_3Ti_2O_7$ were the only two compounds in the train set that showed residuals greater than 10 kJ mol $^{-1}$ atom^{-1}. In the training matrix, both compounds are formed by 3 Ca-Multi and 2 Ti-Oct; however, the effect of different oxidation states of Ti (3+ and 4+) has been neglected. Ti^{3+} and Ti^{4+} are both located in octahedral sites [55–57], but Ti^{3+} has a slightly larger ionic radius than Ti^{4+} due to less electron-electron repulsion between Ti and O. Such a change in valence affects the Ti-O bond distance, which further changes the volume of the Ti-Oct and influences the calculations performed by the MPM [58]. Including additional Ti^{3+} and Ti^{4+} octahedra as features to the MPM might help to improve the model, in a similar way to what has been conducted for Fe-Oct and Fe^{3+}-Oct.

As shown in Fig. 5(a), for the enthalpy of formation test set, MPM predictions yield errors generally below 16 kJ mol $^{-1}$ atom^{-1}, whereas PM predictions show residuals that can exceed 20 kJ mol $^{-1}$ atom^{-1}. For the enthalpy test set, MPM calculations for five compounds out of 16 compounds show a moderate increase in residuals compared to values obtained from PM, as follows: $NaFe_2O_3$ (3.53 %), Ca_2SiO_4 (2.73 %), $CaAl_2SiO_6$ (2.23 %), $Li_2Ca_4Si_4O_{13}$ (1.27 %), and Mg_6MnO_8 (0.38 %). The values in parentheses indicate the percentage increase. In addition to containing alkali elements, another common feature among these compounds is the significant distortion of their constituent edge-sharing octahedra, such as Ca-oct, Fe-oct, Fe^{+3}-oct, Al-oct, Mg-oct and Mn-oct [59–64]. This suggests that the NN model struggles to capture this complex structural behavior, likely due to a lack of compounds with similar structural features in the train set.

As illustrated in Fig. 5(b), the entropy residuals back-calculated by MPM are always lower than 1.4 J mol $^{-1}$ K^{-1} atom^{-1}. In contrast, the residuals back-calculated by PM reach values as high as 8.5 J mol $^{-1}$ K^{-1} atom^{-1}. The compounds with the highest deviations back-calculated by MPM are $Ca_3Ti_2O_6$ ($3CaO{\cdot}Ti_2O_3$), Ca_2MnO_4 ($2CaO{\cdot}MnO_2$), and $MgTiO_3$ ($MgO{\cdot}TiO_2$). Similarly, to the explanation given for enthalpy of formation, the model is not able to account for the effect of oxidation state for a single polyhedron, such as in the case of Ti and Mn, where both have a coordination number of 6 (Ti-Oct and Mn-Oct) despite the difference in ionic radius for different valences. Although the model uses Ti-Oct, Mn-Oct, and Mn-Tet for training, selected based on crystal structure information, it does not differentiate between the various valence states of Ti (i.e., +3 and+4) and Mn (i.e., +2 and+4) in each compound. Therefore, the NN might not be able to properly consider the effect of valence in certain cations, which affects the bond distance and, in turn, the polyhedron volume. Similarly to what has been proposed for the enthalpy of formation, the inclusion of new features such as Ti^{3+} and Ti^{4+} octahedra and Mn^{2+} and Ti^{4+} octahedra could enhance the predictivity of the model due to the possibility to differentiate one valence from another.

As shown in Fig. 5(b), for the entropy test set, MPM predictions yield errors generally below 2.53 J mol $^{-1}$ K^{-1} atom^{-1}, whereas PM predictions show residuals that can exceed 4 J mol $^{-1}$ K^{-1} atom^{-1}. The compounds that did not improve were $LiAl_5O_8$, K_2TiO_3, and $Li_4Ti_5O_{12}$,

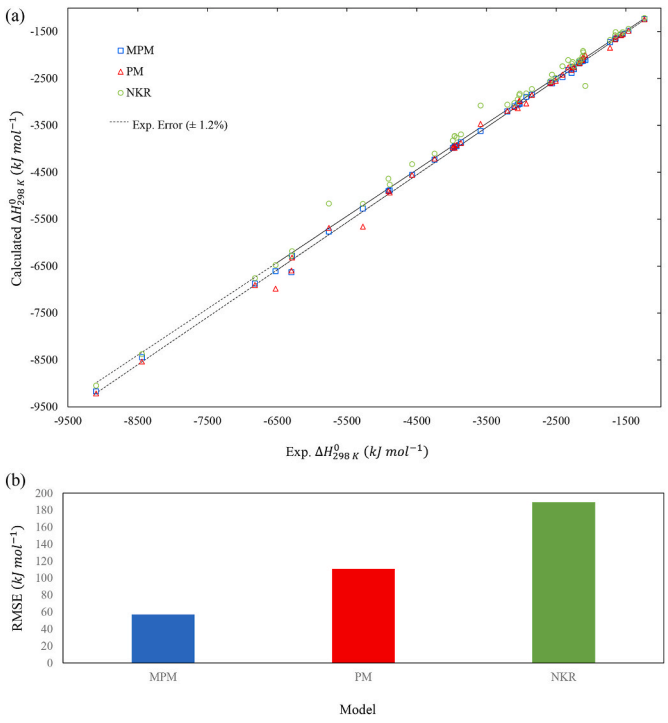

Fig. 6. Comparison of enthalpy of formation calculations for mixed oxides from MPM and PM with experimental values: (a) scatter plot, (b) RMSE metric (values from NKR are also plotted).

among the total of 16 compounds tested. K_2TiO_3 and $Li_4Ti_5O_{12}$ contain Ti^{4+}, which also showed high deviations in the train set and the predictions made for the enthalpy of formation. Furthermore, $LiAl_5O_8$ is an unstable compound under standard conditions, which could affect the comparison between the predictions made by MPM and the properties reported in the literature [65]. Equally to what has been explained for enthalpy of formation in Fig. 5(a), the previously mentioned compounds might include complex behavior related to the valence or sublattice structure that remains overseen by the MPM.

4.2. Comparison with experimental data

By comparing the enthalpy of formation calculations from MPM and PM with experimental data (from the references listed in Table C, appendix), the differences in model precision become more apparent. The experimental data were included in both the train and test sets. Additionally, enthalpy of formation values calculated by NKR are provided to demonstrate the degree of deviation from experimental data.

Fig. 6 compares the experimental enthalpy of formation values for 49 compounds with the enthalpy values calculations from PM, MPM, and NKR. Error bands of 1.2 % have been calculated based on the maximum experimental uncertainty. In Figs. 6(a), 83 % of the MPM calculations fall within the maximum experimental error range, while only 55 % of the PM calculations do. In Fig. 6(b)–a comparison of RMSE values between MPM and PM shows that MPM has the smallest RMSE, which is 49 % lower than PM. The RMSE calculated for NKR was 189.31 kJ mol $^{-1}$.

Fig. 7 shows a comparison of the experimental entropy values for 51 compounds and the calculations performed by MPM, PM, and NKR. The maximum experimental error range reported for entropy is 2.9 %, and error bands corresponding to this value were calculated. In Figs. 7(a), 52 % of the analyzed compounds in MPM fall within the 2.9 % maximum experimental error range, while for PM, only 37 % of the analyzed compounds fall within this range. The comparison of errors for the three models in Fig. 7(b) shows that the RMSE for MPM is smaller compared to

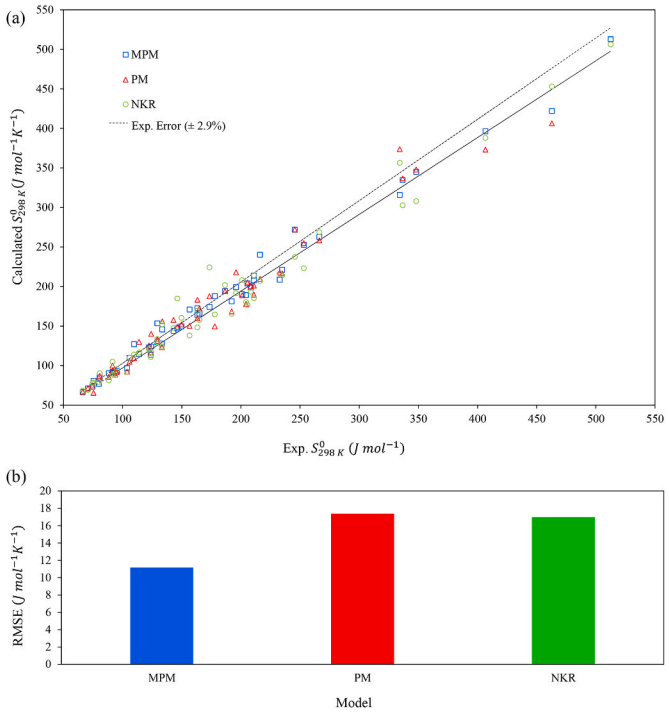

Fig. 7. Comparison of entropy calculations for mixed oxides from MPM, PM, and NKR with experimental values: (a) scatter plot, (b) RMSE metric.

PM and NKR, reducing the error by 36 %. Furthermore, the RMSE reported for NKR is 16.99 J mol $^{-1}$ K^{-1}. The MPM generally improves accuracy by applying a NN correction to the PM model. However, for certain compounds, an opposite behavior is observed. This has been explained in detail in Section 4.1 for some of the compounds.

5. Conclusions

In this work, the Modified Polyhedron Model was developed by combining neural networks with the polyhedron model to estimate the thermodynamic properties of mixed oxides in the Li-Na-K-Ca-Mg-Mn-Fe-Al-Ti-Si-O system. The key findings are summarized below:

- The MPM has achieved significant improvements in alignment with values reported in the literature, reducing the Root Mean Square Error (RMSE) for enthalpy of formation and entropy by 49 % and 36 %, respectively, compared to the PM.
- Approximately 83 % of the MPM calculations fall within the maximum experimental error range for enthalpy of formation, while 52 % of the compounds fall within the maximum experimental error range for entropy, both of which are higher than the values found for PM (i.e., 53 % and 37 % for enthalpy of formation and entropy, respectively).
- The RMSE's for enthalpy of formation and entropy values calculated by NKR are 189.31 kJ mol $^{-1}$ and 16.99 J mol $^{-1}$ K^{-1}, respectively.

Discrepancies in the predictions for certain Ti- and Mn-containing oxides may arise from the model's limited ability to distinguish between multiple oxidation states within a single polyhedron, an approach currently applied only to Fe-octahedra. Explicitly representing oxidation states such as Ti^{3+}, Ti^{4+}, Mn^{2+}, and Mn^{4+} as distinct polyhedron features could help resolve these inconsistencies. Additionally, incorporating features that capture polyhedron distortion may enhance the model's ability to reflect structural variations that significantly influence thermodynamic properties. Moreover, including features like molar volume, which is strongly correlated with entropy but currently underrepresented, could further improve prediction accuracy. As the MPM is inherently data-driven, expanding the training set to encompass a broader range of compounds and polyhedron configurations would enhance both model robustness and generalization, which is currently prevented by the lack of experimental data.

CRediT authorship contribution statement

Jesus A. Arias Hernandez: Writing – review & editing, Writing – original draft, Visualization, Validation, Project administration, Methodology, Investigation, Formal analysis, Data curation. **Elmira Moosavi-Khoonsari:** Writing – review & editing, Writing – original draft, Validation, Supervision, Project administration, Funding acquisition.

Declaration of Competing Interest

The authors declare the following financial interests/personal relationships which may be considered as potential competing interests: Jesus Alejandro Arias Hernandez reports financial support was provided by Natural Sciences and Engineering Research Council of Canada. Elmira Moosavi Khoonsari reports was provided by Natural Sciences and Engineering Research Council of Canada. If there are other authors, they declare that they have no known competing financial interests or personal relationships that could have appeared to influence the work reported in this paper.

Acknowledgements

The authors would like to acknowledge the financial support of NSERC Discovery Grant from the Government of Canada for this project. The authors would like to also sincerely thank Dr. Sunyong Kwon for his invaluable assistance with this project. His contributions have been greatly appreciated and essential to the success of this work.

Appendix D. Supplementary data

Supplementary data to this article can be found online at https://doi.org/10.1016/j.calphad.2025.102848.

Appendix A

Table A(a)
Thermodynamic and physical properties used for training, testing and validating the NN."Dataset" values are after extracting the excess properties from the corresponding values in "Database".

Name	Formula	N	T_c (K)	S_{max} $\left(Jmol^{-1}K^{-1}\right)$	S^{ex}_{-298K} $\left(Jmol^{-1}K^{-1}\right)$	H_{max} $\left(Jmol^{-1}K^{-1}\right)$	H^{ex}_{-298K} $\left(Jmol^{-1}K^{-1}\right)$	Database $\Delta H^{o}_{298\ K}$ $\left(Jmol^{-1}K^{-1}\right)$	Source	Dataset $\Delta H^{o}_{298\ K}$ $\left(Jmol^{-1}K^{-1}\right)$	Database $S^{o}_{298\ K}$ $\left(Jmol^{-1}K^{-1}\right)$	Source	Dataset $S^{o}_{298\ K}$ $\left(Jmol^{-1}K^{-1}\right)$
	Al2Si2O7	11						−3211220.00	FToxid	−3211220.00	136.44	FToxid	136.44
Sillimanite	Al2SiO5	8	2200 [21]	4.00 [21]	0.28		42.34	−2587770.00	FactPS	−2587812.34	95.79	FactPS	91.50
	Al2TiO5	8						−2577173.79	FToxid	−2577173.79	128.44	FToxid	128.44
	Al4TiO8	13						−4194883.42	FToxid	−4194883.42	211.57	FToxid	211.57
Mullite	Al6Si2O13	21						−6819209.98	FactPS	−6819209.98	274.90	FactPS	274.90
Gehlenite	Ca2Al2SiO7	12	700 [21]	11.00 [21]	2.66		415.17	−3985858.32	FToxid	−3986273.48	198.59	FToxid	184.93
	Ca2Fe2O5	9	40 [23]	13.38 [23]				−2131139.00	FToxid	−2131139.00	188.90	FToxid	175.52
	Ca2FeSi2O7	12	40 [23]	13.38 [23]				−3549097.20	FToxid	−3549097.20	215.08	FToxid	201.70
Akermannite	Ca2MgSi2O7	12						−3866291.19	FToxid	−3866291.19	212.00	FToxid	212.00
	Ca2Mn3O8	13	40 [23]	44.69 [23]				−2971100.00	FToxid	−2971100.00	333.50	FToxid	288.80
	Ca2MnO4	7	40 [23]	14.90 [23]				−1899200.00	FToxid	−1899200.00	132.90	FToxid	118.00
Larnite	Ca2SiO4	7	1710 [21]	10.00 [21]	0.91		138.21	−2307513.66	FToxid	−2307651.87	119.65	FToxid	108.74
	Ca3Al2O6	11						−3587266.85	FToxid	−3587266.85	204.17	FToxid	204.17
	Ca3Al2Si3O12	20						−6634443.28	FToxid	−6634443.28	255.14	FToxid	255.15
Andradite	Ca3Fe2Si3O12	20	150 [21]	29.79 [21]		2979.34		−5769999.00	FToxid	−5772978.33	316.35	FToxid	286.55
	Ca3MgAl4O10	18						−5971169.98	FToxid	−5971169.98	241.84	FToxid	241.84
Merwinite	Ca3MgSi2O8	14						−4555779.10	FToxid	−4555779.10	251.77	FToxid	251.77
Rankinite	Ca3Si2O7	12						−3950432.17	FToxid	−3950432.17	205.55	FToxid	205.55
Wollastonite	Ca3Si3O9	15						−4904029.26	FToxid	−4904029.26	239.44	FToxid	239.44
	Ca3SiO5	9						−2857014.90	FToxid	−2857014.90	235.64	FToxid	235.64
	Ca3Ti2O6	11						−3579296.15	FToxid	−3579296.15	212.61	FToxid	212.61
	Ca3Ti2O7	12						−3963479.98	FToxid	−3963479.98	234.72	FToxid	234.72
	Ca4Mn3O10	17	40 [23]	44.69 [23]				−4377500.00	FToxid	−4377500.00	339.50	FToxid	294.80
	Ca4Ti3O10	17						−5619560.00	[23]	−5619560.00	325.00	[23]	325.00
	CaAl12O19	32						−10704185.77	FToxid	−10704185.77	388.91	FToxid	388.91
	CaAl2O4	7						−2324157.82	FToxid	−2324157.82	115.06	FToxid	115.06

Table A(b)
Thermodynamic and physical properties used for training, testing and validating the NN. "Dataset" values are after extracting the excess properties from the corresponding values in "Database".

Name	Formula	N	T_c (K)	S_{max} $\left(Jmol^{-1}K^{-1}\right)$	S^{ex}_{-298K} $\left(Jmol^{-1}K^{-1}\right)$	H_{max} $\left(Jmol^{-1}K^{-1}\right)$	H^{ex}_{-298K} $\left(Jmol^{-1}K^{-1}\right)$	Database $\Delta H^{o}_{298\ K}$ $\left(Jmol^{-1}K^{-1}\right)$	Source	Dataset $\Delta H^{o}_{298\ K}$ $\left(Jmol^{-1}K^{-1}\right)$	Database $S^{o}_{298\ K}$ $\left(Jmol^{-1}K^{-1}\right)$	Source	Dataset $S^{o}_{298\ K}$ $\left(Jmol^{-1}K^{-1}\right)$
Anorthite	CaAl2Si2O8	13	2300 [21]	11.00 [21]	0.74		111.13	−4231594.26	FToxid	−4231705.39	200.18	FToxid	188.44
Ca-tschermaks	CaAl2SiO6	10						−3296800.00	FToxid	−3296800.00	144.50	FToxid	144.50
	CaAl4O7	12						−3999688.87	FToxid	−3999688.87	177.82	FToxid	177.82
Ca-walstromite (ps-wolastonite)	CaCa2(Si3O9)	15						−4876519.68	FToxid	−4876519.68	260.80	FToxid	260.80
	CaFe2O4	7						−1477615.00	FToxid	−1477615.00	145.86	FToxid	145.86
	CaFe4O7	12						−2268796.10	FToxid	−2268796.10	264.80	FToxid	264.8
Hedenbergite	CaFeSi2O6	10	31 [21]	13.38 [21]		276.54		−2843455.80	FToxid	−2843732.33	170.29	FToxid	156.90
Diopside	CaMgSi2O6	10						−3199746.68	FToxid	−3199746.68	142.50	FToxid	142.50
Monticellite	CaMgSiO4	7						−2254211.50	FactPS	−2254211.5	108.30	FactPS	108.30
	CaMn2O4	7						−1737300.00	FToxid	−1737300.00	111.00	FToxid	111.00
	CaMn3O6	10	40 [23]	44.69 [23]				−2245300.00	FToxid	−2245300.00	201.31	FToxid	156.62
	CaMn4O8	13	40 [23]	59.59 [23]				−2753317.00	FToxid	−2753317.00	291.57	FToxid	231.98
	CaMnO3	5	40 [23]	14.90 [23]				−1237000.00	FToxid	−1237000.00	101.75	FToxid	86.85
Perovskite	CaTiO3	5						−1660630.02	FToxid	−1660630.02	93.63	FToxid	93.63
Sphene	CaTiSiO5	8						−2597431.46	FToxid	−2597431.46	129.29	FToxid	129.29
Ferrocordierite	Fe2Al4Si5O18	29	1800 [21]	26.76 [21]	1.73		350.20	−8439257.19	FToxid	−8439607.39	463.49	FToxid	435.00
Ferrosillite	Fe2Si2O6	10	40 [23]	26.76 [23]		713.65		−2390739.52	FToxid	−2391453.16	191.76	FToxid	165.00
Fayalite	Fe2SiO4	7	126 [66]	26.76 [66]		2247.99		−1481938.53	FToxid	−1484186.51	150.93	FToxid	124.16
Ulvöspinel	Fe2TiO4	7	120 [66]	26.76 [66]		2140.94		−1515609.69	FToxid	−1517750.62	168.87	FToxid	142.10
	Fe2TiO5	8						−1738786.72	FactPS	−1738786.72	171.96	FactPS	171.96
Fe-sapphirine (793)	Fe3.5Al9Si1.5O20	34	40 [23]	46.83 [23]		1248.88		−9834581.00	[23]	−9835829.88	504.20	[23]	457.36
Almandine	Fe3Al2Si3O12	18						−5276337.00	FToxid	−5276337.00	336.30	FToxid	336.30
Ferropseudobrookite	FeTi2O5	8	40 [23]	13.38 [23]		356.82		−2152814.44	FToxid	−2153171.26	176.56	FToxid	163.18
Ilmenite	FeTiO3	5	40 [23]	13.38 [23]		356.82		−1233142.16	FToxid	−1233498.98	108.62	FToxid	95.24
	K2Ca6Si4O15	27						−8555000.00	FToxid	−8555000.00	490.49	FToxid	490.49
	K2MgSi5O12	20						−5922850.00	FToxid	−5922850.00	359.10	FToxid	359.10

Table A(c)
Thermodynamic and physical properties used for training, testing and validating the NN. "Dataset" values are after extracting the excess properties from the corresponding values in "Database".

Name	Formula	N	T_c (K)	S_{max} $\left(Jmol^{-1}K^{-1}\right)$	S^{ex}_{-298K} $\left(Jmol^{-1}K^{-1}\right)$	H_{max} $\left(Jmol^{-1}K^{-1}\right)$	H^{ex}_{-298K} $\left(Jmol^{-1}K^{-1}\right)$	Database $\Delta H^{o}_{298\ K}$ $\left(Jmol^{-1}K^{-1}\right)$	Source	Dataset $\Delta H^{o}_{298\ K}$ $\left(Jmol^{-1}K^{-1}\right)$	Database $S^{o}_{298\ K}$ $\left(Jmol^{-1}K^{-1}\right)$	Source	Dataset $S^{o}_{298\ K}$ $\left(Jmol^{-1}K^{-1}\right)$
Potassium disilicate	K2Si2O5	9						−2503700.00	FToxid	−2503700.00	190.58	FToxid	190.58
	K2Si4O9	15						−4342000.00	FToxid	−4342000.00	265.68	FToxid	265.68
Potassium metasilicate	K2SiO3	6						−1543800.00	FToxid	−1543800.00	146.14	FToxid	146.14
	K2Ti2O5	9						−2554500.00	FToxid	−2554500.00	202.92	FToxid	202.92
	K2Ti3O7	12						−3522600.00	FToxid	−3522600.00	253.38	FToxid	253.38
	K2Ti6O13	21						−6392300.00	FToxid	−6392300.00	404.76	FToxid	404.76
	K2TiO3	6						−1555500.00	FToxid	−1555500.00	152.46	FToxid	152.46
	K2TiSi2O7	12						−3433568.86	FToxid	−3433568.86	243.51	FToxid	243.51
	K2TiSi4O11	18						−5262233.13	FToxid	−5262233.13	334.56	FToxid	334.56
	K2TiSiO5	9						−2517743.73	FToxid	−2517743.73	197.98	FToxid	197.98
	K3LiSiO4	9						−2128025.00	FToxid	−2128025.00	213.35	FToxid	213.35
	K4CaSi3O9	17						−4745000.00	FToxid	−4745000.00	380.00	FToxid	380.00
	K4CaSi6O15	26						−7509000.00	FToxid	−7509000.00	564.00	FToxid	564.00
	K4SiO4	9						−2045900.00	FToxid	−2045900.00	245.47	FToxid	245.47
	K6MgO4	11						−1696230.00	FToxid	−1696230.00	333.00	FToxid	333.00
	K8CaSi10O25	44						−12580000.00	FToxid	−12580000.00	897.00	FToxid	897.00
	K8Ti5O14	27						−7251500.00	FToxid	−7251500.00	660.32	FToxid	660.32
Leucite	KAlSi2O6	10	938 [21]	18 [21]	3.13		481.44	−3040080.00	FToxid	−3040561.44	198.50	FToxid	177.36
Hollandite	KAlSi3O8	13						−3962900.00	FToxid	−3962900.00	239.68	FToxid	239.68
Microcline	KAlSi3O8	13						−3962900.00	FToxid	−3962900.00	239.68	FToxid	239.68
Kalsilite	KAlSiO4	7						−2123354.98	FToxid	−2123354.98	134.50	FToxid	134.51
Virgilite	Li(AlSi2O6)	10						−3030516.96	FToxid	−3030516.96	154.20	FToxid	154.20
Petalite	Li(AlSi4O10)	16						−4886099.88	FToxid	−4886099.88	209.60	FToxid	209.60
	Li2Ca2Si2O7	13						−3970313.66	FToxid	−3970313.66	199.41	FToxid	199.41
	Li2Ca3Si6O16	27						−8376100.00	FToxid	−8376100.00	407.61	FToxid	407.61
	Li2Ca4Si4O13	23						−7236000.00	FToxid	−7236000.00	357.77	FToxid	357.77

Table A(d)
Thermodynamic and physical properties used for training, testing and validating the NN. "Dataset" values are after extracting the excess properties from the corresponding values in "Database".

Name	Formula	N	T_c (K)	S_{max} $\left(Jmol^{-1}K^{-1}\right)$	S^{ex}_{-298K} $\left(Jmol^{-1}K^{-1}\right)$	H_{max} $\left(Jmol^{-1}K^{-1}\right)$	H^{ex}_{-298K} $\left(Jmol^{-1}K^{-1}\right)$	Database $\Delta H^{o}_{298\ K}$ $\left(Jmol^{-1}K^{-1}\right)$	Source	Dataset $\Delta H^{o}_{298\ K}$ $\left(Jmol^{-1}K^{-1}\right)$	Database $S^{o}_{298\ K}$ $\left(Jmol^{-1}K^{-1}\right)$	Source	Dataset $S^{o}_{298\ K}$ $\left(Jmol^{-1}K^{-1}\right)$
	Li2CaSiO4	8						−2313755.92	FToxid	−2313755.92	118.32	FToxid	118.33
	Li2MgSiO4	8						−2249815.24	FToxid	−2249815.24	105.50	FToxid	105.50
Lithium disilicate	Li2Si2O5	9						−2559998.98	FToxid	−2559998.98	122.59	FToxid	122.59
Lithium metasilicate	Li2SiO3	6						−1647800.00	FToxid	−1647800.00	79.75	FToxid	79.75
Ramsdellite	Li2Ti3O7	12						−3540500.00	FToxid	−3540500.00	200.00	FToxid	200.00
	Li2TiO3	6						−1670671.00	FToxid	−1670671.00	91.63	FToxid	91.63
	Li2TiSiO5	9						−2601549.99	FToxid	−2601549.99	130.21	FToxid	130.21
	Li3NaSiO4	9						−2278209.00	FToxid	−2278209.00	136.70	FToxid	136.70
	Li4SiO4	9						−2314400.00	FToxid	−2314400.00	117.00	FToxid	117.00
	Li4Ti5O12	21						−6180810.00	FToxid	−6180810.00	328.08	FToxid	328.08
	Li4TiO4	9						−2287300.00	FToxid	−2287300.00	126.24	FToxid	126.24
	Li5AlO4	10						−2383984.00	FToxid	−2383984.00	128.00	FToxid	128.00
	Li6Si2O7	15						−3923190.00	FToxid	−3923190.00	227.02	FToxid	227.02
	Li8SiO6	15						−3515120.00	FToxid	−3515120.00	192.00	FToxid	192.00
Spodumene	LiAl(Si2O6)	10						−3060,000	FToxid	−3060000.00	131.00	FToxid	131.00
Eucryptite	LiAl(SiO4)	7						−2126524.1	FToxid	−2126524.10	96.60	FToxid	96.60
	LiAl5O8	14						−4553500.99	FToxid	−4553500.99	149.75	FToxid	149.75
	LiFeO2	4	40 [23]	13.38 [23]				−750200.00	FactPS	−750200.00	75.31	FactPS	61.93
Cordierite	Mg2Al4Si5O18	29	1800 [21]	20.00 [21]	1.73		261.72	−9167727.00	FToxid	−9167988.71	417.97	FToxid	396.23
Enstatite (ortho-enstatite)	Mg2Si2O6	10						−3090159.58	FToxid	−3090159.58	133.31	FToxid	133.31
Forsterite	Mg2SiO4	7						−2177699.28	FToxid	−2177699.28	94.00	FToxid	94.00
Qandilite	Mg2TiO4	7	40 [23]	6.00 [23]		160.00		−2155788.22	FToxid	−2155948.22	116.17	FToxid	110.17
Pyrope	Mg3Al2Si3O12	20						−6286547.45	FToxid	−6286547.45	266.35	FToxid	266.35
Sapphirine	Mg4Al10Si2O23	39						−12790590.24	FToxid	−12790590.24	452.85	FToxid	452.85
	Mg6MnO8	15	40 [23]	14.90 [23]				−4184000.00	FToxid	−4184000.00	214.50	FToxid	199.60
	MgAl2O4	7						−2300312.69	FactPS	−2300312.69	84.53	FactPS	84.53

Table A(e)
Thermodynamic and physical properties used for training, testing and validating the NN. "Dataset" values are after extracting the excess properties from the corresponding values in "Database".

Name	Formula	N	T_c (K)	S_{max} $\left(Jmol^{-1}K^{-1}\right)$	S^{ex}_{-298K} $\left(Jmol^{-1}K^{-1}\right)$	H_{max} $\left(Jmol^{-1}K^{-1}\right)$	H^{ex}_{-298K} $\left(Jmol^{-1}K^{-1}\right)$	Database $\Delta H^{o}_{298\ K}$ $\left(Jmol^{-1}K^{-1}\right)$	Source	Dataset $\Delta H^{o}_{298\ K}$ $\left(Jmol^{-1}K^{-1}\right)$	Database $S^{o}_{298\ K}$ $\left(Jmol^{-1}K^{-1}\right)$	Source	Dataset $S^{o}_{298\ K}$ $\left(Jmol^{-1}K^{-1}\right)$
Mg-tschermak	MgAl2SiO6	10						−3181144.00	[23]	−3181144.00	139.80	[23]	139.80
	MgSiO3	5						−1545079.79	FToxid	−1545079.79	66.65	FToxid	66.65
Karooite	MgTi2O5	8						−2504887.10	FToxid	−2504887.10	137.34	FToxid	137.34
Geikielite	MgTiO3	5						−1571552.11	FToxid	−1571552.11	74.55	FToxid	74.56
Mn-cordierite	Mn2Al4Si5O18	29	1800 [21]	20 [21]	1.73		261.72	−8747113.14	FToxid	−8747374.85	448.92	FToxid	427.18
Tephroite	Mn2SiO4	7	40 [23]	29.79 [23]		794.49		−1724663.63	FToxid	−1725458.12	163.19	FToxid	133.40
Tetragonal	Mn2TiO4	7	77 [21]	29.79 [21]		1529.39		−1745005.19	FToxid	−1746534.58	169.45	FToxid	139.65
	Mn3Al2Si3O12	20	40 [23]	44.69 [23]				−5662394.48	FToxid	−5662394.48	366.88	FToxid	322.19
Rhodonite	Mn5Si5O15	25	40 [23]	74.48 [23]		1986.22		−6607453.35	FToxid	−6609439.57	512.50	FToxid	438.01
	MnAl2O4	7	40 [23]	14.90 [23]				−2084283.00	FToxid	−2084283.00	113.36	FToxid	98.46
Pyroxmangite	MnSiO3	5	40 [23]	14.90 [23]		397.24		−1321490.67	FToxid	−1321887.91	102.50	FToxid	87.60
Mn-pseudobrookite	MnTi2O5	8	40 [23]	14.90 [23]		397.24		−2286501.14	FToxid	−2286898.38	163.66	FToxid	148.76
Pyrophanite	MnTiO3	5	40 [23]	14.90 [23]		397.24		−1363253.81	FToxid	−1363651.05	104.03	FToxid	89.13
	Na10SiO7	15						−3179680.00	FToxid	−3179680.00	600.00	FToxid	600.00
	Na2Ca3Si6O16	27						−8388448.00	FToxid	−8388448.00	396.00	FToxid	396.00
	Na2Ca8Al6O18	34						−10889098.68	FToxid	−10889098.68	540.83	FToxid	540.83
	Na2CaSi5O12	20						−5924256.79	FToxid	−5924256.79	351.74	FToxid	351.74
	Na2CaSiO4	8						−2268059.45	FToxid	−2268059.45	110.64	FToxid	110.64
	Na2FeO2	5	40 [23]	13.38 [23]				−755435.00	FToxid	−755435.00	134.00	FToxid	120.61
	Na2FeSiO4	8	40 [23]	13.38 [23]				−1820259.00	FToxid	−1820259.00	180.08	FToxid	166.69
	Na2Mg2Si6O15	25						−7442000.00	FToxid	−7442000.00	392.85	FToxid	392.85
	Na2Mg5Si12O30	49						−14830968.25	FToxid	−14830968.25	733.59	FToxid	733.59
	Na2MgSiO4	8						−2184549.00	FToxid	−2184549.00	144.91	FToxid	144.91
Sodium disilicate	Na2Si2O5	9						−2470070.00	FToxid	−2470070.00	165.70	FToxid	165.70
	Na2SiO3	6						−1560430.00	FToxid	−1560430.00	113.80	FToxid	113.80
	Na2Ti2O5	9						−2531320.00	FToxid	−2531320.00	173.63	FToxid	173.63

Table A(f)
Thermodynamic and physical properties used for training, testing and validating the NN. "Dataset" values are after extracting the excess properties from the corresponding values in "Database".

Name	Formula	N	T_c (K)	S_{max} $\left(Jmol^{-1}K^{-1}\right)$	$S^{ex}_{\sim 298K}$ $\left(Jmol^{-1}K^{-1}\right)$	H_{max} $\left(Jmol^{-1}K^{-1}\right)$	$H^{ex}_{\sim 298K}$ $\left(Jmol^{-1}K^{-1}\right)$	Database $\Delta H^{o}_{298\ K}$ $\left(Jmol^{-1}K^{-1}\right)$	Source	Dataset $\Delta H^{o}_{298\ K}$ $\left(Jmol^{-1}K^{-1}\right)$	Database $S^{o}_{298\ K}$ $\left(Jmol^{-1}K^{-1}\right)$	Source	Dataset $S^{o}_{298\ K}$ $\left(Jmol^{-1}K^{-1}\right)$
	Na2Ti3O7	12						−3484853.60	FToxid	−3484853.60	235.14	FToxid	235.14
	Na2Ti6O13	21						−6325789.60	FToxid	−6325789.60	399.86	FToxid	399.86
	Na2TiO3	6						−1554774.40	FToxid	−1554774.40	122.17	FToxid	122.17
	Na2TiSi2O7	12						−3432843.30	FToxid	−3432843.30	216.56	FToxid	216.56
	Na2TiSi4O11	18						−5261507.50	FToxid	−5261507.50	307.61	FToxid	307.61
	Na2TiSiO5	9						−2517018.10	FToxid	−2517018.10	171.04	FToxid	171.04
	Na3Fe5O9	17						−2899490.50	FToxid	−2899490.50	375.36	FToxid	375.36
	Na3FeO3	7	40 [23]	13.38 [23]				−1175870.69	FToxid	−1175870.69	133.43	FToxid	120.05
	Na4Fe6O11	21						−3559339.00	FToxid	−3559339.00	490.54	FToxid	490.54
	Na4FeO3	8						−1205000.00	FToxid	−1205000.00	212.62	FToxid	212.62
Sodium orthosilicate	Na4SiO4	9						−2112000.00	FToxid	−2112000.00	198.81	FToxid	198.81
	Na5FeO4	10						−1450245.79	FToxid	−1450245.79	240.62	FToxid	240.62
	Na5FeSi4O12	22						−5691690.33	FToxid	−5691690.33	422.71	FToxid	422.71
Sodium silicate	Na6Si2O7	15						−3623700.00	FToxid	−3623700.00	345.00	FToxid	345.00
Monophyllosilicate	Na6Si8O19	33						−9187800.00	FToxid	−9187800.00	636.50	FToxid	636.50
	Na8Fe2O7	17						−2710378.00	FToxid	−2710378.00	437.96	FToxid	437.96
	Na8Ti5O14	27						−7218655.20	FToxid	−7218655.20	552.53	FToxid	552.53
	NaAl9O14	24						−7858666.90	FToxid	−7858666.90	285.15	FToxid	285.15
	NaAlO2	4						−1133190.00	FToxid	−1133190.00	70.40	FToxid	70.40
	NaAlSi2O6	10						−3032892.02	FToxid	−3032892.02	144.77	FToxid	144.77
Albite	NaAlSi3O8	13	950 [21]	16.00 [21]	2.75		421.79	−3947955.44	FToxid	−3948377.22	214.32	FToxid	195.57
Nepheline	NaAlSiO4	7	467 [21]	10.00 [21]	3.99		642.89	−2113380.24	FToxid	−2114023.13	125.52	FToxid	111.53
	NaFe2O3	6						−968000.00	FToxid	−968000.00	149.99	FToxid	149.99
	NaFeO2	4	40 [23]	13.38 [23]				−697308.16	FToxid	−697308.16	88.38	FToxid	75.00
Aegirine (Acmite)	NaFeSi2O6	10	50 [21]	14.90 [21]		496.56		−2590525.00	FToxid	−2591021.55	171.00	FToxid	156.10

Table B(a)
List of compounds and their constituent polyhedra used in MPM.

Name	Formula	Ti-oct	Si-tet	Al-tet	Al-oct	Fe3-oct	Fe-tet	Fe-oct	Mn-tet	Mn-oct	Mg-tet	Mg-oct	Ca-oct	Ca-multi	Li-tet	Li-oct	Li-multi	Na-Multi	K-multi	Ref
	Al2Si2O7	0	2	1	1	0	0	0	0	0	0	0	0	0	0	0	0	0	0	67
Sillimanite	Al2SiO5	0	1	1	1	0	0	0	0	0	0	0	0	0	0	0	0	0	0	68
	Al2TiO5	1	0	0	2	0	0	0	0	0	0	0	0	0	0	0	0	0	0	23
	Al4TiO8	1	0	2	2	0	0	0	0	0	0	0	0	0	0	0	0	0	0	23
Mullite	Al6Si2O13	0	2	0	6	0	0	0	0	0	0	0	0	0	0	0	0	0	0	24
Gehlenite	Ca2Al2SiO7	0	1	2	0	0	0	0	0	0	0	0	0	2	0	0	0	0	0	23
	Ca2Fe2O5	0	0	0	0	1	1	0	0	0	0	0	0	2	0	0	0	0	0	69
	Ca2FeSi2O7	0	2	0	0	0	0	1	0	0	0	0	0	2	0	0	0	0	0	70
Akermannite	Ca2MgSi2O7	0	2	0	0	0	0	0	0	0	1	0	0	2	0	0	0	0	0	23
	Ca2Mn3O8	0	0	0	0	0	0	0	0	3	0	0	0	2	0	0	0	0	0	71
	Ca2MnO4	0	0	0	0	0	0	0	0	1	0	0	0	2	0	0	0	0	0	72
Larnite	Ca2SiO4	0	1	0	0	0	0	0	0	0	0	0	2	0	0	0	0	0	0	23
	Ca3Al2O6	0	0	2	0	0	0	0	0	0	0	0	0	3	0	0	0	0	0	73
	Ca3Al2Si3O12	0	3	0	2	0	0	0	0	0	0	0	0	3	0	0	0	0	0	74
Andradite	Ca3Fe2Si3O12	0	3	0	0	2	0	0	0	0	0	0	0	3	0	0	0	0	0	23
	Ca3MgAl4O10	0	0	0	4	0	0	0	0	0	1	0	0	3	0	0	0	0	0	75
Merwinite	Ca3MgSi2O8	0	2	0	0	0	0	0	0	0	0	1	3	0	0	0	0	0	0	23
Rankinite	Ca3Si2O7	0	2	0	0	0	0	0	0	0	0	0	0	3	0	0	0	0	0	23
Wollastonite	Ca3Si3O9	0	3	0	0	0	0	0	0	0	0	0	3	0	0	0	0	0	0	23
	Ca3SiO5	0	1	0	0	0	0	0	0	0	0	0	0	3	0	0	0	0	0	76
	Ca3Ti2O6	2	0	0	0	0	0	0	0	0	0	0	0	3	0	0	0	0	0	77
	Ca3Ti2O7	2	0	0	0	0	0	0	0	0	0	0	0	3	0	0	0	0	0	77
	Ca4Mn3O10	0	0	0	0	0	0	0	0	3	0	0	0	4	0	0	0	0	0	78

Table B(b)
List of compounds and their constituent polyhedra used in MPM.

Name	Formula	Ti-oct	Si-tet	Al-tet	Al-oct	Fe3-oct	Fe-tet	Fe-oct	Mn-tet	Mn-oct	Mg-tet	Mg-oct	Ca-oct	Ca-multi	Li-tet	Li-oct	Li-multi	Na-Multi	K-multi	Ref
	Ca4Ti3O10	3	0	0	0	0	0	0	0	0	0	0	0	4	0	0	0	0	0	24
	CaAl12O19	0	0	6	6	0	0	0	0	0	0	0	0	1	0	0	0	0	0	79
	CaAl2O4	0	0	2	0	0	0	0	0	0	0	0	0	1	0	0	0	0	0	80
Anorthite	CaAl2Si2O8	0	2	2	0	0	0	0	0	0	0	0	1	0	0	0	0	0	0	23
Ca-tschermaks	CaAl2SiO6	0	1	1	1	0	0	0	0	0	0	0	1	0	0	0	0	0	0	23
	CaAl4O7	0	0	4	0	0	0	0	0	0	0	0	0	1	0	0	0	0	0	81
Ca-walstromite (ps-wolastonite)	CaCa2(Si3O9)	0	3	0	0	0	0	0	0	0	0	0	2	1	0	0	0	0	0	23
	CaFe2O4	0	0	0	0	2	0	0	0	0	0	0	0	1	0	0	0	0	0	82
	CaFe4O7	0	0	0	0	4	0	0	0	0	0	0	0	1	0	0	0	0	0	83
Hedenbergite	CaFeSi2O6	0	2	0	0	0	0	1	0	0	0	0	1	0	0	0	0	0	0	23
Diopside	CaMgSi2O6	0	2	0	0	0	0	0	0	0	0	1	1	0	0	0	0	0	0	23
Monticellite	CaMgSiO4	0	1	0	0	0	0	0	0	0	0	1	1	0	0	0	0	0	0	23
	CaMn2O4	0	0	0	0	0	0	0	0	2	0	0	0	1	0	0	0	0	0	84
	CaMn3O6	0	0	0	0	0	0	0	0	3	0	0	0	1	0	0	0	0	0	85
	CaMn4O8	0	0	0	0	0	0	0	0	4	0	0	1	0	0	0	0	0	0	85
	CaMnO3	0	0	0	0	0	0	0	0	1	0	0	0	1	0	0	0	0	0	86
Perovskite	CaTiO3	1	0	0	0	0	0	0	0	0	0	0	0	1	0	0	0	0	0	23
Sphene	CaTiSiO5	1	1	0	0	0	0	0	0	0	0	0	0	1	0	0	0	0	0	23
Ferrocordierite	Fe2Al4Si5O18	0	5	4	0	0	0	2	0	0	0	0	0	0	0	0	0	0	0	23
Ferrosillite	Fe2Si2O6	0	2	0	0	0	0	2	0	0	0	0	0	0	0	0	0	0	0	23
Fayalite	Fe2SiO4	0	1	0	0	0	0	2	0	0	0	0	0	0	0	0	0	0	0	23
Ulvöspinel	Fe2TiO4	1	0	0	0	0	1	1	0	0	0	0	0	0	0	0	0	0	0	24
	Fe2TiO5	1	0	0	0	2	0	0	0	0	0	0	0	0	0	0	0	0	0	55

Table B(c)
List of compounds and their constituent polyhedra used in MPM.

Name	Formula	Ti-oct	Si-tet	Al-tet	Al-oct	Fe3-oct	Fe-tet	Fe-oct	Mn-tet	Mn-oct	Mg-tet	Mg-oct	Ca-oct	Ca-multi	Li-tet	Li-oct	Li-multi	Na-Multi	K-multi	Ref
Fe-sapphirine (793)	Fe3.5Al9Si1.5O20	0	1.5	4.5	4.5	0	0	3.5	0	0	0	0	0	0	0	0	0	0	0	23
	Fe3Al2Si3O12	0	3	0	2	3	0	0	0	0	0	0	0	0	0	0	0	0	0	87
Ferropseudobrookite	FeTi2O5	2	0	0	0	0	0	1	0	0	0	0	0	0	0	0	0	0	0	24
Ilmenite	FeTiO3	1	0	0	0	0	0	1	0	0	0	0	0	0	0	0	0	0	0	24
	K2Ca6Si4O15	0	4	0	0	0	0	0	0	0	0	0	0	6	0	0	0	0	2	88
	K2MgSi5O12	0	5	0	0	0	0	0	0	0	1	0	0	0	0	0	0	0	2	89
Potassium disilicate	K2Si2O5	0	2	0	0	0	0	0	0	0	0	0	0	0	0	0	0	0	2	24
	K2Si4O9	0	4	0	0	0	0	0	0	0	0	0	0	0	0	0	0	0	2	24
Potassium metasilicate	K2SiO3	0	1	0	0	0	0	0	0	0	0	0	0	0	0	0	0	0	2	23
	K2Ti2O5	2	0	0	0	0	0	0	0	0	0	0	0	0	0	0	0	0	2	85
	K2Ti3O7	3	0	0	0	0	0	0	0	0	0	0	0	0	0	0	0	0	2	56
	K2Ti6O13	6	0	0	0	0	0	0	0	0	0	0	0	0	0	0	0	0	2	57
	K2TiO3	1	0	0	0	0	0	0	0	0	0	0	0	0	0	0	0	0	2	90
	K2TiSi2O7	1	2	0	0	0	0	0	0	0	0	0	0	0	0	0	0	0	2	85
	K2TiSi4O11	1	4	0	0	0	0	0	0	0	0	0	0	0	0	0	0	0	2	85
	K2TiSiO5	1	1	0	0	0	0	0	0	0	0	0	0	0	0	0	0	0	2	85
	K3LiSiO4	0	1	0	0	0	0	0	0	0	0	0	0	0	1	0	0	0	3	91
	K4CaSi3O9	0	3	0	0	0	0	0	0	0	0	0	1	0	0	0	0	0	4	92
	K4CaSi6O15	0	6	0	0	0	0	0	0	0	0	0	1	0	0	0	0	0	4	93
	K4SiO4	0	1	0	0	0	0	0	0	0	0	0	0	0	0	0	0	0	4	94
	K6MgO4	0	0	0	0	0	0	0	0	0	0	1	0	0	0	0	0	0	6	95
	K8CaSi10O25	0	10	0	0	0	0	0	0	0	0	0	0	1	0	0	0	0	8	96
	K8Ti5O14	5	0	0	0	0	0	0	0	0	0	0	0	0	0	0	0	0	8	85

Table B(d)
List of compounds and their constituent polyhedra used in MPM.

Name	Formula	Ti-oct	Si-tet	Al-tet	Al-oct	Fe3-oct	Fe-tet	Fe-oct	Mn-tet	Mn-oct	Mg-tet	Mg-oct	Ca-oct	Ca-multi	Li-tet	Li-oct	Li-multi	Na-Multi	K-multi	Ref
Leucite	KAlSi2O6	0	2	1	0	0	0	0	0	0	0	0	0	0	0	0	0	0	1	23
Hollandite	KAlSi3O8	0	3	0	1	0	0	0	0	0	0	0	0	0	0	0	0	0	1	97
Microcline	KAlSi3O8	0	3	1	0	0	0	0	0	0	0	0	0	0	0	0	0	0	1	23
Kalsilite	KAlSiO4	0	1	1	0	0	0	0	0	0	0	0	0	0	0	0	0	0	1	23
Virgilite	Li(AlSi2O6)	0	2	1	0	0	0	0	0	0	0	0	0	0	0	0	1	0	0	23
Petalite	Li(AlSi4O10)	0	4	1	0	0	0	0	0	0	0	0	0	0	0	0	1	0	0	23
	Li2Ca2Si2O7	0	2	0	0	0	0	0	0	0	0	0	0	2	1	0	1	0	0	98
	Li2Ca3Si6O16	0	6	0	0	0	0	0	0	0	0	0	0	3	1	0	1	0	0	85
	Li2Ca4Si4O13	0	4	0	0	0	0	0	0	0	0	0	0	4	0	0	2	0	0	85
	Li2CaSiO4	0	1	0	0	0	0	0	0	0	0	0	0	1	2	0	0	0	0	99
	Li2MgSiO4	0	1	0	0	0	0	0	0	0	1	0	0	0	1	0	1	0	0	100
Lithium disilicate	Li2Si2O5	0	2	0	0	0	0	0	0	0	0	0	0	0	2	0	0	0	0	24
Lithium metasilicate	Li2SiO3	0	1	0	0	0	0	0	0	0	0	0	0	0	2	0	0	0	0	101
Ramsdellite	Li2Ti3O7	3	0	0	0	0	0	0	0	0	0	0	0	0	2	0	0	0	0	23
	Li2TiO3	1	0	0	0	0	0	0	0	0	0	0	0	0	1	1	0	0	0	24
	Li2TiSiO5	1	1	0	0	0	0	0	0	0	0	0	0	0	0	0	2	0	0	102
	Li3NaSiO4	0	1	0	0	0	0	0	0	0	0	0	0	0	1.5	0	1.5	1	0	85
	Li4SiO4	0	1	0	0	0	0	0	0	0	0	0	0	0	0	0	4	0	0	103
	Li4Ti5O12	5	0	0	0	0	0	0	0	0	0	0	0	0	0	0	4	0	0	104
	Li4TiO4	1	0	0	0	0	0	0	0	0	0	0	0	0	0	0	4	0	0	105
	Li5AlO4	0	0	1	0	0	0	0	0	0	0	0	0	0	5	0	0	0	0	106
	Li6Si2O7	0	2	0	0	0	0	0	0	0	0	0	0	0	3	0	3	0	0	107

Table B(e)
List of compounds and their constituent polyhedra used in MPM.

Name	Formula	Ti-oct	Si-tet	Al-tet	Al-oct	Fe3-oct	Fe-tet	Fe-oct	Mn-tet	Mn-oct	Mg-tet	Mg-oct	Ca-oct	Ca-multi	Li-tet	Li-oct	Li-multi	Na-Multi	K-multi	Ref
	Li8SiO6	0	1	0	0	0	0	0	0	0	0	0	0	0	0	0	8	0	0	108
Spodumene	LiAl(Si2O6)	0	2	0	1	0	0	0	0	0	0	0	0	0	0	1	0	0	0	23
Eucryptite	LiAl(SiO4)	0	1	0	1	0	0	0	0	0	0	0	0	0	1	0	0	0	0	23
	LiAl5O8	0	0	2.5	2.5	0	0	0	0	0	0	0	0	0	0	1	0	0	0	85
	LiFeO2	0	0	0	0	0	0	1	0	0	0	0	0	0	0	1	0	0	0	109
Cordierite	Mg2Al4Si5O18	0	5	4	0	0	0	0	0	0	0	2	0	0	0	0	0	0	0	23
Enstatite (ortho-enstatite)	Mg2Si2O6	0	2	0	0	0	0	0	0	0	0	2	0	0	0	0	0	0	0	23

(*continued on next page*)

Table B(e) (*continued*)

Name	Formula	Ti-oct	Si-tet	Al-tet	Al-oct	Fe3-oct	Fe-tet	Fe-oct	Mn-tet	Mn-oct	Mg-tet	Mg-oct	Ca-oct	Ca-multi	Li-tet	Li-oct	Li-multi	Na-Multi	K-multi	Ref
Forsterite	Mg2SiO4	0	1	0	0	0	0	0	0	0	0	2	0	0	0	0	0	0	0	23
Qandilite	Mg2TiO4	1	0	0	0	0	0	0	0	0	1	1	0	0	0	0	0	0	0	24
Pyrope	Mg3Al2Si3O12	0	3	1	1	0	0	0	0	0	0	3	0	0	0	0	0	0	0	24
Sapphirine	Mg4Al10Si2O23	0	2	5	5	0	0	0	0	0	0	4	0	0	0	0	0	0	0	110
	Mg6MnO8	0	0	0	0	0	0	0	0	1	0	6	0	0	0	0	0	0	0	111
	MgAl2O4	0	0	0	2	0	0	0	0	0	1	0	0	0	0	0	0	0	0	112
Mg-tschermak	MgAl2SiO6	0	1	1	1	0	0	0	0	0	0	1	0	0	0	0	0	0	0	23
	MgSiO3	0	1	0	0	0	0	0	0	0	0	1	0	0	0	0	0	0	0	113
Karooite	MgTi2O5	2	0	0	0	0	0	0	0	0	0	1	0	0	0	0	0	0	0	24
Geikielite	MgTiO3	1	0	0	0	0	0	0	0	0	0	1	0	0	0	0	0	0	0	24
Mn-cordierite	Mn2Al4Si5O18	0	5	4	0	0	0	0	0	2	0	0	0	0	0	0	0	0	0	23
Tephroite	Mn2SiO4	0	1	0	0	0	0	0	0	2	0	0	0	0	0	0	0	0	0	23
Tetragonal	Mn2TiO4	1	0	0	0	0	0	0	1	1	0	0	0	0	0	0	0	0	0	24
	Mn3Al2Si3O12	0	3	0	2	0	0	0	0	3	0	0	0	0	0	0	0	0	0	74

Table B(f)
List of compounds and their constituent polyhedra used in MPM.

Name	Formula	Ti-oct	Si-tet	Al-tet	Al-oct	Fe3-oct	Fe-tet	Fe-oct	Mn-tet	Mn-oct	Mg-tet	Mg-oct	Ca-oct	Ca-multi	Li-tet	Li-oct	Li-multi	Na-Multi	K-multi	Ref
Rhodonite	Mn5Si5O15	0	5	0	0	0	0	0	0	5	0	0	0	0	0	0	0	0	0	23
	MnAl2O4	0	0	0	2	0	0	0	1	0	0	0	0	0	0	0	0	0	0	114
Pyroxmangite	MnSiO3	0	1	0	0	0	0	0	0	1	0	0	0	0	0	0	0	0	0	23
Mn-pseudobrookite	MnTi2O5	2	0	0	0	0	0	0	0	1	0	0	0	0	0	0	0	0	0	24
Pyrophanite	MnTiO3	1	0	0	0	0	0	0	0	1	0	0	0	0	0	0	0	0	0	23
	Na10SiO7	0	1	0	0	0	0	0	0	0	0	0	0	0	0	0	0	10	0	23
	Na2Ca3Si6O16	0	6	0	0	0	0	0	0	0	0	0	0	3	0	0	0	2	0	115
	Na2Ca8Al6O18	0	0	6	0	0	0	0	0	0	0	0	0	8	0	0	0	2	0	23
	Na2CaSi5O12	0	5	0	0	0	0	0	0	0	0	0	0	1	0	0	0	2	0	23
	Na2CaSiO4	0	1	0	0	0	0	0	0	0	0	0	0	1	0	0	0	2	0	116
	Na2FeO2	0	0	0	0	0	1	0	0	0	0	0	0	0	0	0	0	2	0	23
	Na2FeSiO4	0	1	0	0	0	1	0	0	0	0	0	0	0	0	0	0	2	0	117
	Na2Mg2Si6O15	0	6	0	0	0	0	0	0	0	2	0	0	0	0	0	0	2	0	118
	Na2Mg5Si12O30	0	12	0	0	0	0	0	0	0	5	0	0	0	0	0	0	2	0	85
	Na2MgSiO4	0	1	0	0	0	0	0	0	0	1	0	0	0	0	0	0	2	0	119
Sodium disilicate	Na2Si2O5	0	2	0	0	0	0	0	0	0	0	0	0	0	0	0	0	2	0	24
	Na2SiO3	0	1	0	0	0	0	0	0	0	0	0	0	0	0	0	0	2	0	120
	Na2Ti2O5	2	0	0	0	0	0	0	0	0	0	0	0	0	0	0	0	2	0	85
	Na2Ti3O7	3	0	0	0	0	0	0	0	0	0	0	0	0	0	0	0	2	0	121
	Na2Ti6O13	6	0	0	0	0	0	0	0	0	0	0	0	0	0	0	0	2	0	24
	Na2TiO3	1	0	0	0	0	0	0	0	0	0	0	0	0	0	0	0	2	0	24

Table B(g)
List of compounds and their constituent polyhedra used in MPM.

Name	Formula	Ti-oct	Si-tet	Al-tet	Al-oct	Fe3-oct	Fe-tet	Fe-oct	Mn-tet	Mn-oct	Mg-tet	Mg-oct	Ca-oct	Ca-multi	Li-tet	Li-oct	Li-multi	Na-Multi	K-multi	Ref
	Na2TiSi2O7	1	2	0	0	0	0	0	0	0	0	0	0	0	0	0	0	2	0	24
	Na2TiSi4O11	1	4	0	0	0	0	0	0	0	0	0	0	0	0	0	0	2	0	23
	Na2TiSiO5	1	1	0	0	0	0	0	0	0	0	0	0	0	0	0	0	2	0	122
	Na3Fe5O9	0	0	0	0	5	0	0	0	0	0	0	0	0	0	0	0	3	0	123
	Na3FeO3	0	0	0	0	0	1	0	0	0	0	0	0	0	0	0	0	3	0	124
	Na4Fe6O11	0	0	0	0	6	0	0	0	0	0	0	0	0	0	0	0	4	0	23
	Na4FeO3	0	0	0	0	1	0	0	0	0	0	0	0	0	0	0	0	4	0	125
Sodium orthosilicate	Na4SiO4	0	1	0	0	0	0	0	0	0	0	0	0	0	0	0	0	4	0	24
	Na5FeO4	0	0	0	0	1	0	0	0	0	0	0	0	0	0	0	0	5	0	126
	Na5FeSi4O12	0	4	0	0	1	0	0	0	0	0	0	0	0	0	0	0	5	0	127
Sodium silicate	Na6Si2O7	0	2	0	0	0	0	0	0	0	0	0	0	0	0	0	0	6	0	24
Monophyllosilicate	Na6Si8O19	0	8	0	0	0	0	0	0	0	0	0	0	0	0	0	0	6	0	24
	Na8Fe2O7	0	0	0	0	2	0	0	0	0	0	0	0	0	0	0	0	8	0	124
	Na8Ti5O14	5	0	0	0	0	0	0	0	0	0	0	0	0	0	0	0	8	0	24
	NaAl9O14	0	0	4.5	4.5	0	0	0	0	0	0	0	0	0	0	0	0	1	0	128
	NaAlO2	0	0	1	0	0	0	0	0	0	0	0	0	0	0	0	0	1	0	129
Jadeite	NaAlSi2O6	0	2	1	0	0	0	0	0	0	0	0	0	0	0	0	0	1	0	130
Albite	NaAlSi3O8	0	3	1	0	0	0	0	0	0	0	0	0	0	0	0	0	1	0	23
Nepheline	NaAlSiO4	0	1	1	0	0	0	0	0	0	0	0	0	0	0	0	0	1	0	23
	NaFe2O3	0	0	0	0	2	0	0	0	0	0	0	0	0	0	0	0	1	0	131

(*continued on next page*)

Table B(g) (*continued*)

Name	Formula	Ti-oct	Si-tet	Al-tet	Al-oct	Fe3-oct	Fe-tet	Fe-oct	Mn-tet	Mn-oct	Mg-tet	Mg-oct	Ca-oct	Ca-multi	Li-tet	Li-oct	Li-multi	Na-Multi	K-multi	Ref
	NaFeO2	0	0	0	0	0	0	1	0	0	0	0	0	0	0	0	0	1	0	85
Aegirine (Acmite)	NaFeSi2O6	0	2	0	0	1	0	0	0	0	0	0	0	0	0	0	0	1	0	23

Appendix C

Table C(a)
Experimental references for $\Delta H^{o}_{298\ K}$ and $S^{o}_{298\ K}$ used for models' comparison.

Name	Formula	Exp. ref. $\Delta H^{o}_{298\ K}$	Exp. ref. $S^{o}_{298\ K}$
	Al2Si2O7	[132]	[132]
Sillimanite	Al2SiO5	[133]	
	Al2TiO5		[134]
	Al4TiO8		
Mullite	Al6Si2O13	[135]	
Gehlenite	Ca2Al2SiO7	[135–137]	[135,136,138]
	Ca2Fe2O5	[139]	
	Ca2FeSi2O7		
Akermannite	Ca2MgSi2O7	[137,140]	[138,140]
	Ca2Mn3O8		
	Ca2MnO4		
Larnite	Ca2SiO4	[141–143]	[135,141,144]
	Ca3Al2O6		[145]
	Ca3Al2Si3O12	[146]	
Andradite	Ca3Fe2Si3O12	[41,147]	[41,147]
	Ca3MgAl4O10		
Merwinite	Ca3MgSi2O8	[148]	[138]
Rankinite	Ca3Si2O7	[142,149]	[135,144]
Wollastonite	Ca3Si3O9	[141,142]	[135,141,150]
	Ca3SiO5	[143]	
	Ca3Ti2O6		
	Ca3Ti2O7		[134]
	Ca4Mn3O10		
	Ca4Ti3O10		
	CaAl12O19		
	CaAl2O4		
Anorthite	CaAl2Si2O8	[141]	[141,144]
Ca-tschermaks	CaAl2SiO6		

Table C(b)
Experimental references for $\Delta H^{o}_{298\ K}$ and $S^{o}_{298\ K}$ used for models' comparison.

Name	Formula	Exp. ref. $\Delta H^{o}_{298\ K}$	Exp. ref. $S^{o}_{298\ K}$
	CaAl4O7		[145]
Ca-walstromite (ps-wolastonite)	CaCa2(Si3O9)		
	CaFe2O4		
	CaFe4O7		
Hedenbergite	CaFeSi2O6	[151]	[42,144,151]
Diopside	CaMgSi2O6	[135]	[150]
Monticellite	CaMgSiO4	[148]	
	CaMn2O4		
	CaMn3O6		
	CaMn4O8		
	CaMnO3		
Perovskite	CaTiO3	[152]	[153]
Sphene	CaTiSiO5		[154]
Ferrocordierite	Fe2Al4Si5O18	[155]	[155,156]
Ferrosillite	Fe2Si2O6		[43]
Fayalite	Fe2SiO4	[141,157]	[141,158]
Ulvöspinel	Fe2TiO4		[159]
	Fe2TiO5		[159]
Fe-sapphirine (793)	Fe3.5Al9Si1.5O20		
Almandine	Fe3Al2Si3O12	[160]	
Ferropseudobrookite	FeTi2O5		
Ilmenite	FeTiO3	[152]	[153]
	K2Ca6Si4O15		
	K2MgSi5O12		

(*continued on next page*)

Table C(b) (*continued*)

Name	Formula	Exp. ref. $\Delta H^{o}_{298\ K}$	Exp. ref. $S^{o}_{298\ K}$
Potassium disilicate	K2Si2O5		
	K2Si4O9		
Potassium metasilicate	K2SiO3		[161]
	K2Ti2O5		
	K2Ti3O7		
	K2Ti6O13		

Table C(c)
Experimental references for $\Delta H^{o}_{298\ K}$ and $S^{o}_{298\ K}$ used for models' comparison.

Name	Formula	Exp. ref. $\Delta H^{o}_{298\ K}$	Exp. ref. $S^{o}_{298\ K}$
	K2TiO3		
	K2TiSi2O7		
	K2TiSi4O11		
	K2TiSiO5		
	K3LiSiO4		
	K4CaSi3O9		
	K4CaSi6O15		
	K4SiO4		
	K6MgO4		
	K8CaSi10O25		
	K8Ti5O14		
Leucite	KAlSi2O6	[141,162,163]	[141,164]
Hollandite	KAlSi3O8		
Microcline	KAlSi3O8	[141,162,165]	[141,164,166]
Kalsilite	KAlSiO4	[141,162,163]	[141,164]
Virgilite	Li(AlSi2O6)	[141]	
Petalite	Li(AlSi4O10)	[167]	[167,168]
	Li2Ca2Si2O7		
	Li2Ca3Si6O16		
	Li2Ca4Si4O13		
	Li2CaSiO4		
	Li2MgSiO4		
Lithium disilicate	Li2Si2O5	[169,170]	[169]
Lithium metasilicate	Li2SiO3	[169,170]	[161,169]
Ramsdellite	Li2Ti3O7		
	Li2TiO3		[134,171]
	Li2TiSiO5		

Table C(d)
Experimental references for $\Delta H^{o}_{298\ K}$ and $S^{o}_{298\ K}$ used for models' comparison.

Name	Formula	Exp. ref. $\Delta H^{o}_{298\ K}$	Exp. ref. $S^{o}_{298\ K}$
	Li3NaSiO4		
	Li4SiO4	[172]	
	Li4Ti5O12		
	Li4TiO4		
	Li5AlO4		
	Li6Si2O7		
	Li8SiO6		
Spodumene	LiAl(Si2O6)	[141,163]	[141,173]
Eucryptite	LiAl(SiO4)	[141,163]	[173]
	LiAl5O8		
	LiFeO2		[139,171]
Cordierite	Mg2Al4Si5O18	[133]	[138,155]
Enstatite (ortho-enstatite)	Mg2Si2O6	[174]	
Forsterite	Mg2SiO4	[133,141,174]	[141]
Qandilite	Mg2TiO4	[152]	
Pyrope	Mg3Al2Si3O12	[133]	[175]
Sapphirine	Mg4Al10Si2O23		
	Mg6MnO8		
	MgAl2O4	[133,174]	[145]
Mg-tschermak	MgAl2SiO6		
	MgSiO3	[174]	
Karooite	MgTi2O5	[152]	
Geikielite	MgTiO3	[152]	[153]
Mn-cordierite	Mn2Al4Si5O18		

Table C(e)
Experimental references for $\Delta H^{o}_{298\ K}$ and $S^{o}_{298\ K}$ used for models' comparison.

Name	Formula	Exp. ref. $\Delta H^{o}_{298\ K}$	Exp. ref. $S^{o}_{298\ K}$
Tephroite	Mn2SiO4	[141,142]	[141]
Tetragonal	Mn2TiO4		
	Mn3Al2Si3O12		
Rhodonite	Mn5Si5O15	[141,142,157]	[141]
	MnAl2O4		
Pyroxmangite	MnSiO3		
Mn-pseudobrookite	MnTi2O5		
Pyrophanite	MnTiO3		
	Na10SiO7		
	Na2Ca3Si6O16		
	Na2Ca8Al6O18		
	Na2CaSi5O12		
	Na2CaSiO4		
	Na2FeO2		
	Na2FeSiO4		
	Na2Mg2Si6O15		
	Na2Mg5Si12O30		
	Na2MgSiO4		
Sodium disilicate	Na2Si2O5	[176]	[176,177]
	Na2SiO3		[177]
	Na2Ti2O5		
	Na2Ti3O7		
	Na2Ti6O13		
	Na2TiO3		

Table C(f)
Experimental references for $\Delta H^{o}_{298\ K}$ and $S^{o}_{298\ K}$ used for models' comparison.

Name	Formula	Exp. ref. $\Delta H^{o}_{298\ K}$	Exp. ref. $S^{o}_{298\ K}$
	Na2TiSi2O7		
	Na2TiSi4O11		
	Na2TiSiO5		
	Na3Fe5O9		
	Na3FeO3		
	Na4Fe6O11		
	Na4FeO3		
Sodium orthosilicate	Na4SiO4	[176]	[176,177]
	Na5FeO4		
	Na5FeSi4O12		
Sodium silicate	Na6Si2O7	[176]	[176]
Monophyllosilicate	Na6Si8O19		
	Na8Fe2O7		
	Na8Ti5O14		
	NaAl9O14		
	NaAlO2		[139,171]
	NaAlSi2O6	[178]	[164]
Albite	NaAlSi3O8	[141,165]	[141,164,166]
Nepheline	NaAlSiO4	[141]	[141,164,179]
	NaFe2O3		[63]
	NaFeO2		[139,171]
Aegirine (Acmite)	NaFeSi2O6		

Data availability

Data will be made available on request.

References

[1] M.J. Sánchez-Rivera, M.J. Orts, V. Pérez-Herranz, S. Mestre, Effect of type and amount of alumina as dopant over the densification and the electrical properties of zinc oxide ceramic electrodes, Bol. Soc. Esp. Ceram V 60 (1) (2021) 8.

[2] D. Zhao, S. Haijun, Y. Liu, Z. Shen, H. Liu, Y. Guo, et al., Ultrahigh-strength porous ceramic composites via a simple directional solidification process, Nano Lett. 22 (6) (2022) 2405–2411.

[3] A. Lucia, O. Gregory, Modeling thermophysical properties of glasses, Sci. Rep. 13 (1) (2023) 989.

[4] M.D. Mashitah, Y.S. Chan, J. Jason, Chapter 8 - antimicrobial properties of nanobiomaterials and the mechanism, in: A.M. Grumezescu (Ed.), Nanobiomaterials in Antimicrobial Therapy, William Andrew Publishing, 2016, pp. 261–312.

[5] I.H. Jung, S.A. Decterov, A.D. Pelton, Critical thermodynamic evaluation and optimization of the MgO-Al2O3, CaO-MgO-Al2O3, MgO-Al2O3-SiO2 systems, JPEDAV. 25 (2004) 17.

[6] I. Irikka, R. Zhang, L-g Xia, N. Hellsten, P.A. Taskinen, Thermodynamic assessment of ZnO-SiO_2 system, Trans. Nonferrous Metals Soc. China 28 (9) (2018) 8.

[7] J.W. Anthony, R.A. Bideaux, K.W. Bladh, M.C. Nichols, Handbook of Mineralogy America MSo, Mineralogical Society of America, USA, 1995.

[8] A. Navrotsky, New developments in the calorimetry of high-temperature materials, Engineering 5 (3) (2019) 366–371.

[9] H. Zhang, H. Wu, DFT studies on the thermodynamic properties of $Na_2Ti_3O_7$ under high temperature and high pressure, Phys. Status Solidi 245 (1) (2008) 37–43.

[10] J. You, J. Wang, S. Zhang, J. Luo, Z. Peng, M. Rao, et al., Thermodynamic properties of Na_2MgSiO_4: DFT calculation and experimental validation, Calphad 79 (2022).

[11] C. Takoukam-Takoundjou, E. Bourasseau, V. Lachet, Study of thermodynamic propertis of $U_{1-y}Pu_yO_2$ MOX fuel using classical molecular Monte Carlo Simulations, J. Nucl. Mater. 534 (2020) 13.

[12] U. Becker Af-G, M. Prieto, R. Harrison, A. Putnis, Direct calculation of thermodynamic properties of the barite-celestite solid solution from molecular principles, Phys. Chem. Miner. 27 (2000) 291–300.

[13] R. Mittal, S. Kumar, M.K. Gupta, S.K. Mishra, S. Mukhopadhyay, Le M. Duc, et al., Sodium diffusion and dynamics in Na2Ti3O7: neutron scattering and ab initio simulations, Mater. Adv. 3 (4) (2022) 2104–2116.

[14] A.J. Cohen PM-S, W. Yang, Limitations to DFT, Science 321 (2008) 792–794.

[15] T. Chen, Q. Liu, Y. Liu, L. Sun, M. Chen, Combining stochastic density functional theory with deep potential molecular dynamics to study warm dense matter, Matter Radiat. Extremes 9 (1) (2024).

[16] W. Latimer, Methods of estimating thermodynamic properties of compounds, J. Am. Chem. Soc. 73 (4) (1951) 1480–1482.

[17] H. Kopp, Investigations of the specific heat of solid bodies, Philos. Trans. Royal Soc. A. 155 (1865) 71–203.

[18] R.G. Berman THB, Heat capacity of minerals in the system Na_2O-K_2O-CaO-MgO-FeO-Fe_2O_3- Al_2O_3-SiO_2- TiO_2- H_2O- CO_2, Contrib. Mineral. Petrol. 89 (1985) 15.

[19] H. Helgeson, J.M. Delany, H.W. Nesbitt, D.K. Bird, Summary and critique of rock forming minerals, Am. J. Sci. (1978).

[20] J.A. Chermak, J.D. Rimstidt, Estimating the thermodynamic properties (ΔG_{fo} and ΔH_{fo}) of silicate minerals at 298 K from the sum of polyhedral contributions, Am. Mineral. 74 (1989) 8.

[21] T.J.B. Holland, Dependence of entropy on volume for silicate and oxide minerals: a review and a predictive model, Am. Mineral. 74 (1989) 5–13.

[22] V.J. Van-Hinsberg, S.P. Vriend, J.C. Schumacher, A new method to calculate end-member thermodynamic properties of minerals from their constituent polyhedra II: heat capacity, compressibility and thermal expansion, J. Metamorph. Geol. 23 (8) (2005) 681–693.

[23] V.J. Van Hinsberg, S.P. Vriend, J.C. Schumacher, A new method to calculate end-member thermodynamic properties of minerals from their constituent polyhedra I: enthalpy, entropy and molar volume, J. Metamorph. Geol. 23 (3) (2005) 165–179.

[24] T. Wu, E. Moosavi-Khoonsari, I.-H. Jung, Estimation of thermodynamic properties of oxide compounds from polyhedron method, Calphad 57 (2017) 107–117.

[25] J.A. Arias-Hernandez, S.Y. Kwon, E. Moosavi-Khoonsari, Application of polyhedron model to predict heat capacity of mixed oxides, SSRN (2024).

[26] L. Pauling, The Nature of the Chemical Bond, Cornell University Press, 1939, p. 664.

[27] H.W. Anderson, L.A. Bromley, A method for estimating the heat of formation of the halides, J. Phys. Chem. 63 (1959) 3.

[28] D.E. Wilcox, L.A. Bromley, Computer estimation of heat and free energy of formation for simple inorganic compounds, Ind. Eng. Chem. 55 (7) (1963) 32–39.

[29] M.W.M. Hisham, S.W. Benson, Empirical relations among the enthalpies of formation of different anionic compounds, J. Phys. Chem. 92 (1988) 6107–6112.

[30] W.S. Fyfe, F.J. Turner, J. Verhoogen, Effect of temperature on equilibrium entropy of solids, Geol. Soc. Am. (1958).

[31] H. Helgeson, Thermodynamic properties of hydrothermal systems at elevated temperatures and pressures, Am. J. Sci. 267 (1969) 75.

[32] G.R. Robinson, J.L. Haas, Heat capacity, relative enthalpy, and calorimetric entropy of silicate minerals: an empirical method of prediction, Am. Mineral. 68 (1983) 12.

[33] R.M. Hanzen, A useful fiction: polyhedron modelling of mineral properties, Am. J. Sci. 228-A (1988) 242–269.

[34] R.M. Hanzen, Comparative Chemical and Polyhedron Approach, 1985.

[35] E. Moosavi-Khoonsari, J.A. Arias-Hernandez, S.Y. Kwon, Review and perspective on polyhedron model for estimating thermodynamic properties of oxides, J. Am. Ceram. Soc. 107 (3) (2024) 1636–1647.

[36] M.A. Carpenter, Thermochemistry of Aluminium/Silicon ordering in feldspar minerals, in: Physical Properties and Thermodynamic Behaviour of Minerals, 225, NATO ASI Series, Netherlands, 1988.

[37] A. La-Iglesia, J. Felix, Estimation of thermodynamic properties of mineral carbonates at high and low temperatures from the sum of polyhedral contributions, Geochem. Cosmochim. Acta 58 (19) (1994) 3983–3991.

[38] M. Fathollahi, H. Sajady, QSPR modeling of decomposition temperature of energetic cocrystals using artificial neural network, J. Therm. Anal. Calorim. 133 (3) (2018) 1663–1672.

[39] J. Nelson, S. Sanvito, Predicting the Curie temperature of ferromagnets using machine learning, Phys. Rev. Mater. 3 (10) (2019) 104405.

[40] R. Powell, T.J.B. Holland, An internally consistent thermodynamic dataset with uncertainties and correlations: 1. Methods and a worked example, J. Metamorph. Geol. 3 (1985) 15.

[41] R. Robie, Z. Bin, B. Hemingway, M. Barton, Heat capacity and thermodynamic properties of andradite garnet $Ca_3Fe_2Si_3O_{12}$ between 10 and 1000 K and revised values for $G_{298.15K}$ of hedenbergite and wollastionite, Geochem. Cosmochim. Acta 51 (1987) 6.

[42] H.T. Haselton, R.A. Robie, B.S. Hemingway, Heat capacities of synthetic hedenbergite, ferrobustamite and $CaFeSi_2O_6$ glass, Geochem. Cosmochim. Acta 51 (8) (1987) 2211–2217.

[43] L. Cemič, E. Dachs, Heat capacity of ferrosilite, $Fe_2Si_2O_6$, Phys. Chem. Miner. 33 (7) (2006) 457–464.

[44] F. Grønvold, A. Sveen, Heat capacity and thermodynamic properties of synthetic magnetite (Fe_3O_4) from 300 to 1050 K. Ferrimagnetic transition and zero-point entropy, J. Chem. Therm. 6 (9) (1974) 859–872.

[45] B. Smetana, M. Žaludová, M. Tkadlečková, J. Dobrovská, S. Zlá, K. Gryc, et al., Experimental verification of hematite ingot mould heat capacity and its direct utilisation in simulation of casting process, J. Therm. Anal. Calorim. 112 (1) (2013) 473–480.

[46] R.A. Lange, I.S.E. Carmichael, J.F. Stebbins, Phase transitions in leucite ($KAlSi_2O_6$), orthorhombic $KAlSiO_4$, and their iron analogues ($KFeSi_2O_6$, $KFeSiO_4$), Am. Mineral. 71 (1986) 8.

[47] H. U, D.R. W, Structural and other contributions to the third-law entropies of silicates, Geochem. Cosmochim. Acta 40 (1976) 24.

[48] H.H. Ulbrich DRW, Structural and other contributions to the third-law entropies of silicates, Geochem. Cosmochim. Acta 40 (1976) 24.

[49] C.-W. Hsu, C.-C. Chang, C.-J. Lin (Eds.), A Practical Guide to Support Vector Classification, APG, 2009.

[50] T. Szandała, Review and comparison of commonly used activation functions for deep neural networks, in: J. Kacprzyk (Ed.), Bio-inspired Neurocomputing, 903, Springer, Poland, 2021, p. 22.

[51] D.P. Kingma, J.L. Ba (Eds.), ADAM: A Method for Stochastic Optimization 3rd International Conference for Learning Representations, 2015. USA.

[52] D. Chicco, Ten quick tips for machine learning in computational biology, BioData Min. 10 (2017) 35.

[53] Z. Peixiang, L. Guoshu, C. Wuxiao, C. Yuqing, H. Zeyan, X. Chenguan, et al., Power data-carbon emission prediction model based on stacking ensemble and hyperparameter optimization with cross-validation method. 2022 First International Conference on Cyber-Energy Systems and Intelligent Energy (ICCSIE), 2023, pp. 1–6.

[54] V. Watts, Introduction to Statistics an Excel-Based Approach, Canada Fanshawe College Pressbooks, 2022.

[55] W. Guo, S. Malus, D. Ryan, Z. Altounian, Crystal structure and cation distribution in the $FeTi_2O_5$-Fe_2TiO_5 solid solution series, J. Phys. Condens. Matter 11 (1999) 9.

[56] FLRe Silva, A.A.A. Filho, M.B. da Silva, K. Balzuweit, J.L. Bantignies, E.W. S. Caetano, et al., Polarized Raman, FTIR, and DFT study of $Na_2Ti_3O_7$ microcrystals, J. Raman Spectrosc. 49 (3) (2018) 538–548.

[57] H. Cid, M. Buerger, The crystal structure of potassium hexatitanate $K_2Ti_6O_{13}$, Z. Kristallogr. 117 (1962) 19.

[58] P.M. Doyle, P.F. Schofield, A.J. Berry, A.M. Walker, K.S. Knight, Substitution of Ti3+ and Ti4+ in hibonite (CaAl12O19), Am. Mineral. 99 (7) (2014) 1369–1382.

[59] M.E. Villafuerte-Castrejon, A. Dago, R. Pomes, Crystal structure determination of $Li_2Ca_4Si_4O_{13}$, J. Solid State Chem. 112 (1994) 3.

[60] A. Baran, J. Barzowska, M. Grinberg, S. Mahlik, K. Szczodrowski, Y. Zorenko, Binding energies of Eu^{2+} and Eu^{3+} ions in β-Ca_2SiO_4 doped with europium, Opt. Mater. 35 (12) (2013) 2107–2114.

[61] S. Udagawa, K. Urabe, M. Natsume, T. Yano, Refinement of the crystal structure of gamma-Ca_2SiO_4, Cement Concr. Res. 10 (1980) 5.

[62] R.L. Flemming, V. Terskikh, E. Ye, Aluminum environments in synthetic Ca-Tschermak clinopyroxene ($CaAlAlSiO_6$) from Rietveld refinement, 27Al NMR, and first-principles calculations, Am. Mineral. 100 (10) (2015) 2219–2230.

[63] S.R. Bruno, C.K. Blakely, V.V. Poltavets, Synthesis of mixed-valent α- and β-$NaFe_2O_3$ polymorphs under controlled partial oxygen pressure, J. Solid State Chem. 192 (2012) 68–74.

[64] H. Taguchi, A. Ohta, M. Nagao, H. Kido, H. Ando, K. Tabata, Crystal structure and magnetic properties of $(Mg_{6-x}Li_x)MnO_8$, J. Solid State Chem. 124 (2) (1996) 220–223.

[65] Q. Chen, H. Wang, P. Xu, B. Tu, X. Zong, K. Zheng, et al., Crystal structure and bond-valence investigation of nitrogen stabilized $LiAl_5O_8$ spinel, Inog Chem. 62 (1) (2022) 6.

[66] R.S. Carmichael, Handbook of Physical Properties of Rocks, CRC Press, Boca Raton, 1982, p. 356.

[67] Y. Zhou, T. Irifune, T. Kuribayashi, Phase relations of the Al_2O_3–SiO_2 system at 13–21 GPa and 2300–2800 K and a new high-pressure $Al_2Si_2O_7$ phase, Phys. Chem. Miner. 48 (7) (2021).

[68] I.J. Kim, L.G. Gauckler, Formation, decoposition and thermal stability of Al_2TiO_5, J. Ceram. Sci. Technol. 3 (2) (2012) 11.

[69] S. Dhankhar, D.S. Vavilapalli, G. Bhalerao, S. Ganesamoorthy, S. Hussain, K. Baskar, et al., Growth of brownmillerite $Ca_2Fe_2O_5$ single crystals under air, oxygen and argon atmospheres using optical floating zone technique: a comparative study, Bull. Mater. Sci. 45 (1) (2022).

[70] L. Bindi, When minerals become complex: an elementary introduction to superspace crystallography to describe natural-occurring incommensurately modulated structures, Rendiconti Lincei 19 (1) (2008) 1–16.

[71] G. Ansell, M. Modrick, Structure of calcium manganese oxide $Ca_2Mn_3O_8$, Acta Crystallogr. B38 (1982) 2.

[72] C. Autret, C. Martin, M. Hervieu, R. Retoux, B. Raveau, G. André, et al., Structural investigation of Ca_2MnO_4 by neutron powder diffraction and electron microscopy, J. Solid State Chem. 177 (6) (2004) 2044–2052.

[73] K.A. Gedekar, S.P. Wankhede, S.V. Moharil, R.M. Belekar, Synthesis, crystal structure and luminescence in $Ca_3Al_2O_6$, J. Mater. Sci. Mater. Electron. 29 (8) (2018) 6260–6265.

[74] C. Geiger, T. Armbruster, $Mn_3Al_2Si_3O_{12}$ spessartine and $Ca_3Al_2Si_3O_{12}$ grossular garnet sructural dynamic and thermodynamic properties, Am. Mineral. 82 (1997) 7.

[75] V. Kahlenberg, Re-investigation and correct symmetry of $Ca_3CoAl_4O_{10}$, Acta Crystallogr E Crystallogr Commun 75 (Pt 2) (2019) 214–217.

[76] M.-N. De-Noirfontaine, F. Dunstetter, M. Courtial, G. Gasecki, M. Signes-Frehel, Tricalcium Silicate Ca_3SiO_5, the major component of anhydrous portlant cement:

on the conservation of distances and direction and their relationship to the structural elements, Z. Kristallogr. 218 (1) (2003) 3.
[77] W. Li, J. Qiu, C. Liu, G. Huo, M. Jiang, Phase equilibria of CaO–Al_2O_3–CaO-TiO_2 system at 1500 °C in hydrogen atmosphere, Ceram. Int. 50 (20) (2024) 38769–38777.
[78] P.D. Battle, M.A. Green, J. Lago, J. Milburn, M. Rosseinsky, J. Venite, Crystal and magnetic structures of $Ca_4Mn_3O_{10}$, a n=3 Ruddlesden-Popper compound, Chem. Mater. 10 (1998) 6.
[79] C. Zhao, Y. Xu, L. Wang, X. Chen, W. Hu, Z. Dai, et al., A remarkably tunable emission from red to yellow to green in Mn^{4+}-activated $CaAl_{12}O_{19}$ phosphor via co-doping Bi^{3+}, J. Mater. Sci. Mater. Electron. 30 (12) (2019) 11419–11428.
[80] E.I. Marchenko, A.R. Oganov, E.A. Mazhnik, N.N. Eremin, Stable compounds in the CaO-Al_2O_3 system at high pressures, Phys. Chem. Miner. 49 (11) (2022).
[81] L. Vasylechko, V. Stadnik, V. Hreb, Y. Zhydachevskyy, A. Luchechko, V. Mykhaylyk, et al., Synthesis, crystal structure and photoluminescent properties of red-emitting $CaAl_4O_7$:Cr^{3+} nanocrystalline phosphor, INORGA 11 (5) (2023).
[82] Z. Que, Surface Structures of $CaFe_2O_4$ (001), (100), (110) and (111): a density functional theory study, ISIJ Int. 61 (5) (2021) 1370–1378.
[83] E. Millon, B. Malaman, A. Bonazebi, J. Brice, R. Gerardin, O. Evrard, Hemicalcic ferrite $CaFe_4O_7$ crystal structure, Mater. Res. Bull. 21 (8) (1986) 9.
[84] B.D. White, C.A. dos-Santos, J.A. Souza, K.J. McClellan, J.J. Neumeier, Crystal growth and characterization of Marokite $CaMn_2O_4$+δ, J. Cryst. Growth 310 (14) (2008) 3325–3330.
[85] A. Jain, S.P. Ong, G. Hautier, W. Chen, W.D. Richards, S. Dacek, et al., Commentary: the Materials Project: a materials genome approach to accelerating materials innovation, APL Mater. 1 (1) (2013).
[86] J. Zagorac, A. Azarubica, A. Radosavljevic-Mihajlovic, D. Zagorac, V. Matovic, Structural study of nanosized ytrrium doped $CaMnO_3$ perovskites, Bull. Mater. Sci. 37 (3) (2014) 9.
[87] D. Zherebetskyy, S. Lebernegg, G. Amthauer, M. Grodzicki, Magnetic structure of almandine, Phys. Chem. Miner. 39 (2012) 10.
[88] E. Arroyabe, R. Kaindl, D.M. Többens, V. Kahlenberg, $K_2Ca_6Si_4O_{15}$—structural and spectroscopical studies on a mixed tetrahedral–octahedral framework, J. Solid State Chem. 182 (12) (2009) 3254–3261.
[89] A. Bell, C. Henderson, S. Redfern, R. Cernik, P. Champness, A. Fitch, et al., Structures of synthetic $K_2MgSi_5O_{12}$ leucites by integrated X ray powder diffraction, electron diffraction and Si MAS NMR methods, Acta Crystallogr. B50 (1994) 10.
[90] H.S. Khalsa, M.D. Smith, H.C. zur Loye, Crystal growth and structure determination of K_2TiO_3: a five coordinate titanate, Mater. Res. Bull. 44 (1) (2009) 91–94.
[91] R. Hoffmann, R. Hoppe, Ein lithosilicat K_3LiSiO_4=$K_3[LiSiO_4]$, Z. Anorg. Allg. Chem. 560 (1988) 11.
[92] E. Arroyabe, R. Kaindl, V. Kahlenberg, Structural and Raman spectroscopic investigations of $K_4BaSi_3O_9$ and $K_4CaSi_3O_9$, Z. Anorg. Allg. Chem. 635 (2) (2009) 337–345.
[93] H. Liu, E. Hildebrandt, H. Krammer, V. Kahlenberg, H. Krüger, H. Schottenberger, $K_4CaSi_6O_{15}$—solving a 90-year-old riddle, J. Am. Ceram. Soc. 104 (12) (2021) 6678–6695.
[94] K. Bernet, R. Hoppe, Zur kristallstruktur von $K_4[SiO_4]$, Z. Anorg. Allg. Chem. 589 (1990) 9.
[95] B. Darriet, M. Devalette, F. Roulleau, M. Avallet, Structure cristalline de K_6MgO_4, Acta Crystallogr. 30 (11) (1975) 3.
[96] H. Liu, H. Krammer, V. Kahlenberg, H. Krüger, C. Hejny, E. Dachs, et al., $K_8CaSi_{10}O_{25}$ – synthesis, in-situ high-temperature single-crystal diffraction and heat capacity, J. Solid State Chem. 334 (2024).
[97] J. Zhang, J. Ko, R.M. Hazen, C.T. Prewitt, High-pressure crystal chemistry of $KAlSi_3O_8$ hollandite, Am. Mineral. 78 (5–6) (1993) 493–499.
[98] V. Kahlenberg, E. Brunello, C. Hejny, H. Krüger, D. Schmidmair, M. Tribus, et al., $Li_2Ca_2Si_2O_7$: structural, spectroscopic and computational studies on a sorosilicate, J. Solid State Chem. 225 (2015) 155–167.
[99] J.A. Gard, A.R. West, Preparation and crystal structure of Li_2CaSiO, and isostructual Li_2CaGeO_4, J. Solid State Chem. 7 (1973) 5.
[100] C. Jousseaume, A. Kahn-Harari, D. Vivien, J. Derouet, F. Ribot, F. Villain, Structural and spectroscopic characterisation of Cr:Li_2MgSiO_4 (γ_0), J. Mater. Chem. 12 (5) (2002) 1525–1529.
[101] N.T. Han, V.K. Dien, M.-F. Lin, Excitonic effects in the optical spectra of Li_2SiO_3 compound, Sci. Rep. 11 (1) (2021) 7683.
[102] Y. Wu, Z. Xu, Y. Liu, J. Chen, L. Peng, O.J. Borkiewicz, et al., Electronic structure of anode material Li_2TiSiO_5 and its structural evolution during lithiation, J. Phys. Chem. C 125 (7) (2021) 3733–3744.
[103] Y. Deng, C. Eames, J.-N. Chotard, F. Lalère, V. Seznec, S. Emge, et al., Structural and mechanistic insights into fast lithium-ion conduction in Li_4SiO_4–Li_3PO_4 solid electrolytes, J. Am. Chem. Soc. 137 (28) (2015) 9136–9145.
[104] K. Kataoka, Y. Takahashi, N. Kijima, J. Akimoto, K-i Ohshima, Single crystal growth and structure refinement of $Li_4Ti_5O_{12}$, J. Phys. Chem. Solid. 69 (5) (2008) 1454–1456.
[105] R.P. Gunawardane, J.G. Fletcher, M.A. Dissanayake, R.A. Howie, A.R. West, Crystal structure refinement of Li_4TiO_4 containing tetrahedrally coordinated Ti4+ and tetragonally packed oxide ions, J. Solid State Chem. 112 (1) (1994) 70–72.
[106] D. Okuda, H. Kobayashi, M. Ishikawa, Electrochemical characteristics of Co-substituted alpha- and beta-Li_5AlO_4 as high-specific capacity positive electrode materials, ACS Omega 5 (27) (2020) 16912–16918.
[107] H. Völlenkle, A. Wittmann, H. Nowotny, Zur Kristallstruktur von $CuGeO_3$, Monatshefte für Chemie und verwandte Teile anderer Wissenschaften 98 (4) (1967) 1352–1357.
[108] Y. Duan, H. Pfeiffer, B. Li, I.C. Romero-Ibarra, D.C. Sorescu, D.R. Luebke, et al., CO_2 capture properties of lithium silicates with different ratios of Li_2O/SiO_2: an ab initio thermodynamic and experimental approach, Phys. Chem. Chem. Phys. 15 (32) (2013) 13538–13558.
[109] R. Akiyama, Y. Ikedo, M. Månsson, T. Goko, J. Sugiyama, D. Andreica, et al., Short-range spin correlations in beta-LiFeO2 from bulk magnetization, neutron diffraction, and mu-SR experiments, Phys. Rev. B 81 (2) (2010) 024404.
[110] J. Barbier, Crystal structures of sapphirine and surinamite analogues in the MgO-Ga_2O_3-GeO_2 system, Eur. J. Mineral 10 (6) (1998) 1283–1293.
[111] J. Kasper, J. Prener, The crystal structure of Mg_6MnO_8, Acta Crystallogr. 7 (1954) 3.
[112] N. Obradovic, S. Filipovic, W. Fahrenholtz, B. Marinkovic, J. Rogan, S. Levic, et al., Morphological and structural characterization of $MgAl_2O_4$ spinel, Sci. Sinter. 55 (1) (2023) 1–10.
[113] E. Ito, Y. Matsui, Synthesis and crystal-chemical characterization of $MgSiO_3$ perovskite, Earth Planet Sci. Lett. 38 (2) (1978) 443–450.
[114] U. Hålenius, F. Bosi, H. Skogby, Galaxite, $MnAl_2O_4$, a spectroscopic standard for tetrahedrally coordinated Mn^{2+} in oxygen-based mineral structures, Am. Mineral. 92 (7) (2007) 1225–1231.
[115] B. Li, K.M. Knowles, Molecular dynamics simulation of twinning in devitrite, $Na_2Ca_3Si_6O_{16}$, Philos. Mag. 93 (13) (2013) 1582–1603.
[116] T.F.W. Barth, E. Posnjak, Silicate structures of the cristobalite type: II, The crystal structure of Na_2CaSiO_4 81 (1–6) (1932) 370–375.
[117] Z. Ye, X. Zhao, S. Li, S. Wu, P. Wu, M.C. Nguyen, et al., Robust diamond-like Fe-Si network in the zero-strain Na_xFeSiO_4 cathode, Electrochim. Acta 212 (2016) 14.
[118] M.E. Cradwick, K.A. Shahid, H.F.W. Taylor, Crystal structure of $Na_2Mg_2Si_6O_{15}$, Nat. Phys. Sci. (Lond.) 236 (68) (1972) 110.
[119] R. Withers, C. Lobo, J. Thompson, S. Schmid, R. Stranger, A modulation wave approach to the structural characterization of three new cristobalite related sodium magnesiosilicates, Acta Crystallogr. B53 (1997) 18.
[120] F. Liu, S.H. Garofalini, R.D. King-Smith, D. Vanderbilt, Structural and electronic properties of sodium metasilicate, Chem. Phys. Lett. 215 (4) (1993) 401–404.
[121] S. Andersson, A. Wadsley, The crystal structure of $Na_2Ti_3O_7$, Acta Crystallogr. 14 (1961) 5.
[122] F. Meng, Y. Liu, L. Wang, D. Chen, H. Zhao, Y. Zhen, et al., Vibrational spectral analysis of natisite (Na_2TiSiO_5) and its structure evolution in water and sulfuric acid solutions, Materials 14 (9) (2021).
[123] C. Romers, C. Rooymans, R. De-Graf, The preparation crystal structure and magnetic properties of $Na_3Fe_5O_9$, Acta Crystallogr. 27 (1967) 6.
[124] M. Sofin, M. Jansen, Synthesis, crystal structure and magnetic properties of β-Na_3FeO_3, Solid State Sci. 8 (1) (2006) 19–23.
[125] R. Hoppe, H. Rieck, Zur Kenntnis von Na_4FeO_3, Z. Anorg. Allg. Chem. 437 (1977) 10.
[126] R.V. Thøgersen, F. Bianchini, H. Fjellvåg, P. Vajeeston, Antifluorite-type Na_5FeO_4 as a low-cost, environment-friendly cathode with combined cationic/anionic redox activity for sodium ion batteries: a first-principles investigation, RSC Adv. 12 (27) (2022) 17410–17421.
[127] M. Ahmadzadeh, T.A. Olds, A. Scrimshire, P.A. Bingham, J.S. McCloy, Structure and properties of $Na_5FeSi_4O_{12}$ crystallized from $5Na_2O$-Fe_2O_3-$8SiO_2$ glass, Acta Crystallogr C Struct Chem. 74 (Pt 12) (2018) 1595–1602.
[128] K.J.D. MacKenzie, M.E. Smith, M. Schmücker, H. Schneider, P. Angerer, Z. Gan, et al., Structural aspects of mullite-type $NaAl_9O_{14}$ studied by 27Al and 23Na solid-state MAS and DOR NMR techniques, Phys. Chem. Chem. Phys. 3 (11) (2001) 2137–2142.
[129] J.A. Kaduk, S. Pei, The crystal structure of hydrated sodium aluminate, $NaAlO_2 \cdot 5/4H_2O$, and its dehydration product, J. Solid State Chem. 115 (1) (1995) 126–139.
[130] C. Prewitt, C. Burnham, The crystal structure of jadeite $NaAlSi_2O_6$, Am. Mineral. (1966).
[131] B. Sobotka, A. Moeller, Zur synthese von Na_3FeO_3 einem ternaeren oxoferrat (III) mit kettenstruktur, Z. Anorg. Allg. Chem. 298 (2003) 3.
[132] R. Robie, B. Hemmingway, Entropies of kyanite, andalusite and sillimanite: additional constraints on the pressure and temperature of the Al_2SiO_5 triple point, Am. Mineral. 69 (1984) 9.
[133] T. Charlu, R. Newton, J. Kleppa, Enthalpies of formation at 970 K of compounds in the system MgO-Al_2O_3-SiO_2 from high temperature solution calorimetry, Geochem. Cosmochim. Acta 39 (1975) 11.
[134] E.G. King, Low-temperature heat capacities and entropies at 298.16 K. of some titanates of aluminum, calcium, lithium and zinc, J. Am. Chem. Soc. 77 (8) (1955) 2150–2152.
[135] G. Eriksson, A.D. Pelton, Critical evaluation and optimization of the thermodynamic properties and phase diagrams of the CaO-Al_2O_3, Al_2O_3-SiO_2, and CaO-Al_2O_3-SiO_2 systems, Metall. Trans. A B 24 (5) (1993) 807–816.
[136] B. Hemingway, R. Robie, Heat capacity and thermodynamic functions for gehlenite and staurolite: with comments on the Schottky anomaly in the heat capacity of staurolite, Am. Mineral. 69 (1984) 12.
[137] T. Charlu, R. Newton, J. Kleppa, Thermochemistry of Synthetic $Ca_2Al_2SiO_7$ (gehlenite) and $Ca_2MgSi_2O_7$ (akermanite) melilites, Geochem. Cosmochim. Acta 45 (1981) 9.
[138] W. Weller, K. Kelley, Low Temperature Heat Capacities and Entropies at 298.15 K of Akermanite, Cordierite, Gehlenite and Merwinite, 6343, Bureau of mines report of investigation, 1963, p. 7.
[139] M. Koehler, R. Barany, K. Kelley, Heats and Free Energies of Formation of Ferrites and Aluminates of Calcium, Magnesium, Sodium and Lithium, 5711, Bureau of mines report of investigation, 1961, p. 14.

[140] B. Hemingway, H. Evans, G. Nord, H. Haselton, R. Robie, J. McCree, Akermanite phase transitions in heat capacity and thermal expansion and revised thermodynamic data, Can. Mineral. 24 (1986) 10.
[141] B. Hemingway, R. Robie, Enthalpies of formation of low albite ($NaAlSi_3O_8$) gibbsite ($Al(OH)_3$) and $NaAlO_2$; revised values for H_{298} and G_{298} of some aluminosilicate minerals, J. Res. U. S. Geol. Surv. 5 (4) (1977) 18.
[142] G. Eriksson, P. Wu, M. Blander, A.D. Pelton, Critical evaluation and optimization of the thermodynamic properties and phase diagrams of the MnO–SiO_2 and CaO–SiO_2 systems, Can. Metall. Q. 33 (1) (1994) 13–21.
[143] E. King, Heats of formation of crystalline calcium orthosilicate, tricalcium silicate and zinc orthosilicate, J. Am. Chem. Soc. 73 (2) (1951) 656–658.
[144] E.G. King, Low temperature heat capacities and entropies at 298.15 K of some crystalline silicates containing calcium, J. Am. Chem. Soc. 79 (20) (1957) 5437–5438.
[145] E.G. King, Heat capacities at low temperatures and entropies at 298.16°K. Of crystalline calcium and magnesium aluminates, J. Phys. Chem. 59 (3) (1955) 218–219.
[146] K. Krupka, R. Robie, B. Hemingway, High temperature heat capacities of corundum, periclase, anorthite, $CaAl_2Si_2O_8$ glass, muscovite, pyrohphyllite, $KAlSi_3O_8$ glass, grossular and $NaAlSi_3O^8$ glass, Am. Mineral. 64 (1979) 16.
[147] Z. Zhang, S. Saxena, Thermodynamic properties of andradite and application to skarn with coexisting andradite and hedenbergite, Contrib. Mineral. Petrol. 107 (1991) 9.
[148] K. Neuvonen, Heat of formation of merwinite and monticellite, Am. J. Small Bus. 8 (1952).
[149] W. Weeks, Heats of formation of metamorphic minerals in the System CaO-MgO-SiO_2-H_2O and their pretrological significance, J. Geol. 64 (5) (1956) 17.
[150] K. Krupka, R. Robie, B. Hemingway, Low temperature heat capacities and derive thermodynamic properties of anthophyllite, diopside, enstatite, bronzite, and wollastonite, Am. Mineral. 70 (1985) 11.
[151] K. Bennington, R. Beyer, R. Brown, Thermodynamic Properties of Hedenbergite a Complex Silicate of Ca, Fe, Mn and Mg, 8873, Bureau of mines report of investigation, 1984, p. 24.
[152] K. Kelley, S. Todd, E. King, Heat and Free Energy Data for Titanates of Iron and the Alkaline-Earth Metals, 5059, Bureau of mines report of investigation, 1954, p. 37.
[153] H. Shomate, Heat capacities at low temperature of the metatitanates of iron, calcium and magnesium, J. Am. Chem. Soc. 68 (6) (1946) 3.
[154] E.G. King, R.L. Orr, K.R. Bonnickson, Low temperature heat capacity, entropy at 298.16° K., and high temperature heat content of sphene ($CaTiSiO_5$), J. Am. Chem. Soc. 76 (17) (1954) 4320–4321.
[155] E. Dachs, C.A. Geiger, Low-temperature heat capacity of synthetic Fe- and Mg-cordierite: thermodynamic properties and phase relations in the system FeO-Al_2O_3-SiO_2-(H_2O), Eur. J. Mineral 20 (1) (2008) 47–62.
[156] C.A. Geiger, H. Voigtländer, The heat capacity of synthetic anhydrous Mg and Fe cordierite, Contrib. Mineral. Petrol. 138 (1) (2000) 46–50.
[157] E. King, Heats of Formation of Manganous Metasilicate (Rhodonite) and Ferrous Orthosilicate (Fayalite), 74, Bureau of mines report of investigation, 1952, p. 3.
[158] R.A. Robie, C.B. Finch, B.S. Hemingway, Heat capacity and entropy of fayalite (Fe_2SiO_4) between 5.1 and 383 K: comparison of calorimetric and equilibrium values for the QFM buffer reaction, Am. Mineral. 67 (5–6) (1982) 463–469.
[159] S.S. Todd, E.G. King, Heat capacities at low temperatures and entropies at 298.16 K. of titanomagnetite and ferric titanate, J. Am. Chem. Soc. 75 (18) (1953) 4547–4549.
[160] E. Dachs, C.A. Geiger, A. Benisek, Almandine: lattice and non-lattice heat capacity behavior and standard thermodynamic properties, Am. Mineral. 97 (2012) 11.
[161] D.R. Stull, D.L. Hildenbrand, F.L. Oetting, G.C. Sinke, Low-temperature heat capacities of 15 inorganic compounds, J. Chem. Eng. Data 15 (1) (1970) 52–56.
[162] D.-G. Kim, B. Konar, I.-H. Jung, Thermodynamic optimization of the K_2O-Al_2O_3-SiO_2 system, Ceram. Int. 44 (14) (2018) 16712–16724.
[163] R. Barany, L. Adami, Heats of Formation of Lithium Solfate and Five Potassium and Lithium Aluminum Silicates, 6873, Bureau of mines report of investigation., 1966, p. 18.
[164] K. Kelley, S. Todd, R. Orr, E. King, Thermodynamic properties of sodium-aluminum and potasium-aluminum silicates, Bur. Mine. Rep. Invest. 4955 (1953) 17.
[165] D.R. Waldbaum, High-temperature thermodynamic properties of alkali feldspars, Contrib. Mineral. Petrol. 17 (1) (1967) 71–77.
[166] R. Openshaw, B. Hemingway, R. Robie, D. Waldbaum, K. Krupka, The heat capacities at low temperatures and entropies at 298.15 K of low albite, analbite, microcline and high sanidine, Journ Research US Geol Survey 4 (2) (1976) 10.
[167] K. Bennington, J. Stuve, M. Ferrante, Thermodynamic Properties of Petalite ($Li_2Al_2Si_8O_{20}$), 8451, Bureau of mines report of investigation, 1980, p. 12.
[168] B. Hemingway, R. Robie, J. Kittrick, E. Grew, J. Nelen, D. London, The heat capacities of osumilite from 298.15 to 100 K the thermodynamic of two natural chlorites to 500 K, and the thermodynamic properties of petalite to 1800 K, Am. Mineral. 69 (1984) 10.
[169] K. Bennington, M. Ferrante, J. Stuve, Thermodynamic Properties of Two Lithium Silicates (Li_2SiO_3 and $Li_2Si_2O_5$) Bureau of Mines Report of Investigation, 8187, 1976, p. 11.
[170] B. Konar, M.-A. Van Ende, I.-H. Jung, Critical evaluation and thermodynamic optimization of the Li-O, and Li_2O-SiO_2 systems, J. Eur. Ceram. Soc. 37 (5) (2017) 2189–2207.
[171] A. Christensen, K. Conway, K. Kelley, High Temperature Heat Contents and Entropies of Aluminates and Ferrites of Lithium and Sodium and Lithium Titanate, 5565, Bureau of mines report of investigation, 1960, p. 7.
[172] H. Ihle, R. Penzhorn, P. Schuster, The thermochemistry of lithium silicates in view of their use as breeder materials Fusion, Eng. Des. 8 (1989) 4.
[173] L. Pankratz, W. Weller, Thermodynamic Properties of Three Lithium-Aliminum Silicates, 7001, Bureau of mines report of investigation, 1967, p. 12.
[174] J. Shearer, J. Kleppa, The enthalpies of formation of $MgAl_2O_4$, $MgSiO_3$, Mg_2SiO_4 and Al_2SiO_5 by oxide melt solution calorimetry, J. Inorg. Nucl. Chem. 35 (1973) 8.
[175] C. Téqui, S. Robie RA, R. Hemingway B, D. Neuville, P. Richet, Melting and thermodynamic properties of pyrope ($Mg_3Al_2Si_3O_{12}$), Geochem. Cosmochim. Acta 55 (4) (1991) 1005–1010.
[176] N.W. McCready, The thermodynamic properties of sodium silicate, J. Phys. Colloid Chem. 52 (8) (1948) 1277–1283.
[177] K.K. Kelley, The specific heats at low temperatures of crystalline Ortho-, Meta-, and Disilicates of sodium, J. Am. Chem. Soc. 61 (2) (1939) 471–473.
[178] B. Hemingway, S. Bohlen, W. Hankins, E. Westrum, O. Kushov, Heat capacity and thermodynamic properties of coesite and jadeite, reexamination of the quartz-coesite equilibrium boundary, Am. Mineral. 83 (1998) 10.
[179] D. de Ligny, P. Richet, Jr EF. Westrum, J. Roux, Heat capacity and entropy of rutile (TiO_2) and nepheline ($NaAlSiO_4$), Phys. Chem. Miner. 29 (4) (2002) 267–272.